

AMERICAN UNIVERSITY OF BEIRUT

PULSED LASER DEPOSITION OF SILICON
CARBIDE THIN FILMS: GROWTH,
BONDING AND THERMAL
CHARACTERIZATION

by

AISHA ZIAD AL RIFAI

A thesis

submitted in partial fulfillment of the requirements
for the degree of Master of Sciences
to the Department of Physics
of the Faculty of Art and Sciences
at the American University of Beirut

Beirut, Lebanon
January 2021

AMERICAN UNIVERSITY OF BEIRUT

PULSED LASER DEPOSITION OF SILICON
CARBIDE THIN FILMS: GROWTH,
BONDING AND THERMAL
CHARACTERIZATION

by
Aisha Ziad Al Rifaii


Approved by:



Dr. Malek Tabbal, Professor

Advisor

Physics



Dr. Michel Kazan, Associate Professor

Member of Committee

Physics



Dr. Mohammad Haidar, Assistant Professor

Member of Committee

Physics

Date of thesis defense: January 28, 2021

AMERICAN UNIVERSITY OF BEIRUT

THESIS, RELEASE FORM

Student Name: Al Rifai Aisha Ziad
Last First Middle

Master's Thesis Master's Project Doctoral Dissertation

I authorize the American University of Beirut to: (a) reproduce hard or electronic copies of my thesis, dissertation, or project; (b) include such copies in the archives and digital repositories of the University; and (c) make freely available such copies to third parties for research or educational purposes.

I authorize the American University of Beirut, to: (a) reproduce hard or electronic copies of it; (b) include such copies in the archives and digital repositories of the University; and (c) make freely available such copies to third parties for research or educational purposes after: **One** **year from the date of submission of my thesis, dissertation or project.**
Two ___ years from the date of submission of my thesis , dissertation or project.
Three ___ years from the date of submission of my thesis , dissertation or project.


Signature

2/8/2021
Date

Acknowledgements

First of all, I would like to thank my advisor, Professor Malek Tabbal, for his patience, motivation, and immense knowledge. His invaluable guidance helped me in all the time of research and writing of this thesis.

Besides my advisor, I would like to thank my thesis committee Prof. Michel Kazan and Dr. Mohammad Haidar for their encouragement and support in terms of communication and availability.

I gratefully acknowledge the financial support from the Abdulla Al Ghurair Foundation for Education (AGFE) that allowed me to pursue my education at AUB through the STEM scholarships program. I also would like to thank Ms Hiba Baalbaki, AGFE coordinator at AUB, for all her support and guidance during my MS studies and, once again, Prof M Tabbal for his management of the AGFE STEM program at AUB.

I'd like to present my sincere thankfulness to my mother and my deceased father whom I lost during my research, for their great role in my life their endless sacrifices for me. Thank you for enduring my persistent resolution not to back down. Your love, support, and acceptance have enabled me to become the person I am today.

Getting through my thesis work required more than academic support, and I have my friends, graduate colleagues, and my family at Al Naqab to thank for all their support, motivation, and being there for me in all my hard times. Especially I would like to thank Sara Sarout, Hind Anan, Carmen Masri, Alaa Akoush, Mohmad Daher, Farah Fahes, Anas Al-Khatib, Ziena Hassan, Assaf Smair, Basil Akari.

I would like also to thank Zeinab Harajli for all her support, guidance, and endless support on all levels. Thank you, Nadia Younes, for being a much-needed source of daily encouragement to see this thesis through.

An Abstract of the Thesis of

Aisha Ziad Al Rifaii for Master of Sciences
Major: Physics

Title: Pulsed laser deposition of silicon carbide thin films: growth, bonding and thermal characterization

Silicon Carbide (SiC), in its crystalline form, is a wide band-gap semiconductor that has attracted much interest as a potential replacement of Si silicon in high power / high temperature devices with a wide range of modern technological fields. Its amorphous counterpart (a-SiC) has also its fair share of applications because of its tuning optical, electronic and mechanical properties. Recently, there has been greater attention directed towards the study of the thermal properties of such materials from both the fundamental and technological aspects. In this thesis, we have achieved the synthesis of silicon carbide thin films on Si substrates by pulsed laser deposition with the aim of investigating their thermal properties as the nano-structure of the films transitions from amorphous to crystalline depending on growth conditions. The effects of the several experimental process parameters (laser repetition rate, growth pressure and temperature) on the nature of the grown films were revealed through several materials characterization techniques. Surface profilometry was used to measure film thickness and growth rate while surface morphology was imaged using Scanning Electron Microscopy (SEM). X-Ray Diffraction (XRD) and Raman Spectroscopy allowed the assessment of crystallinity and the determination of the type of bonding of the films, respectively. We used a photothermal-beam-deflection technique (laser flash) to determine the thermal diffusivity of the grown layers. We were able to develop synthesis process that is reproducible where the growth rate depends almost linearly on laser repetition rate up to 25 Hz. Process controllability becomes problematic at higher repetition rate such as 50 Hz. We have also found that growth rate is significantly reduced at deposition pressures of 10 mTorr and above, due to the scattering of the ablated species by the background Ar gas. Deposition temperature plays a crucial role in determining the bonding configuration in the layers. At 300 °C, the grown layers are amorphous with the onset

of crystallites formation detected at 600 °C. Fully crystallized layers are observed at 950 °C. The thermal diffusivity was determined at the onset of crystallization in the SiC layers, and a value of 1.12 cm²/s was reported, showing a significant enhancement compared to the Si substrate (0.88 cm²/s). These results are very encouraging as they pave the way towards a full investigation of the evolution of the thermal properties of unhydrogenated silicon carbide materials as their nanostructure evolves from an amorphous to a fully crystalline state.

Contents

Acknowledgements	v
Abstract	vi
1 Introduction	1
1.1 Theory of Thermal Transport in Crystalline Materials	1
1.2 Theory of Thermal Transport in Amorphousness Materials	2
2 An Overview of Silicon Carbide & Pulsed Laser Deposition	7
2.1 Silicon Carbide definition	7
2.2 Silicon Carbide unique properties	9
2.2.1 Mechanical properties	9
2.2.2 Electric properties	10
2.2.3 Thermal properties	10
2.3 Pulsed Laser Deposition	10
2.3.1 Mechanism of PLD Process	10
2.3.2 Advantages and Disadvantages of PLD	12
2.4 PLD growth of SiC	12
3 Experimental Techniques	14
3.1 PLD Experimental Setup	14
3.2 Characterization Techniques and Analysis of Thin Films	14
3.2.1 Scanning Electron Microscopy (SEM)	14
3.2.2 Energy-Dispersive X-Ray Spectroscopy (EDX)	16
3.2.3 Raman Spectroscopy	17
3.2.4 X-Ray Diffraction	20
3.2.5 Profilometer	21
3.2.6 Laser Flash	21
4 Results & Discussion	29
4.1 Film Growth Conditions	29
4.2 Thickness and Surface Morphology determination	30
4.2.1 Profilometer Measurements	30

4.2.2	Scanning Electron Microscopy Imaging	33
4.3	Raman Spectroscopy	33
4.4	X-Ray Diffraction	35
4.5	Laser flash measurements	36
5	Conclusion	42

List of Figures

1.1	Calculated thermal conductivity (based on equation 1.2 versus measured at room temperature) [1]	3
1.2	Thermal conductivity versus temperature in amorphous Silicon [2]	4
1.3	Illustration of density of vibrational states of amorphous silicon and the three types of heat carriers [3]	5
2.1	SiC Tetragonal bonding of a Carbon atom with the four nearest Silicon neighbors	8
2.2	Schematic positions of atom centers for a close spherical packing. There are only three possible positions for atom centers—A, B and C [4]	8
2.3	The stacking Sequence of Most Common SiC Polytypes [4]	9
2.4	Schematic of PLD technique	11
3.1	PLD Setup	15
3.2	Cross section representation of the optical elements of the SEM .	16
3.3	Elemental composition report by INCA of one of SiC samples (sample 8)	17
3.4	Rayleigh & Raman scattering (a) Rayleigh scattering (b) Stokes Raman scattering (scattered photon has less energy than the incident photon) and (c) anti-Stokes Raman scattering (scattered photon has more energy than the incident photon).	18
3.5	Raman spectroscopy instrumentation diagram	19
3.6	The measurement obtained by Dektak XT Profilometer	22
3.7	Beam Deflection (BD) signal vs. the relative position (r_0) of the pump and probe beams. The circles are experimental data of the (a) amplitude and (b) phase of the BD signal at the pump beam is translated across the sample (inset image). The solid lines are the slope magnitude and phase calculated from 3.8	25
3.8	The schematic diagram of the experimental set up	26
3.9	Position Sensing Quadratic Detector	27
4.1	Surface profilometry measurements of SiC films deposited on Si substrate (a) at 300 °C and (b) at 600 °C (c) at 950 °C	32

4.2	SEM Images of SiC films deposited on Si substrate (a) at 300 °C and (b) at 600 °C	33
4.3	Raman spectra of SiC films deposited on Si substrate at temperatures 950 °C (sample 14), 600 °C (sample 13), and 300 °C (sample 7)	34
4.4	XRD pattern of SiC films deposited on Si substrate at temperatures 950 °C (sample 14), 600 °C (sample 13), and 300 °C (sample 7)	35
4.5	The (a) magnitude and (b) phase plots for sample 7 at frequency 3500 Hz	36
4.6	The magnitude and phase plots for sample 7 at frequencies 2000,3000, 3500, 4000, 4500, and 5000 Hz	37
4.7	Slope of the phase in the linear region for sample 7 at frequency 3500 Hz	38
4.8	Data of sample 7, deposited at 300 °C	38
4.9	The plot of L_{th}^2 versus $1/\pi.f$ for sample 7, deposited at 300 °C	39
4.10	Data of sample 13, deposited at 600 °C	39
4.11	The plot of L_{th}^2 versus $1/\pi.f$ for sample 13, deposited at 600 °C	40
4.12	Data of sample 14, deposited at 950 °C	40
4.13	The plot of L_{th}^2 versus $1/\pi.f$ for sample 14, deposited at 950 °C	41

List of Tables

2.1	Comparison of the properties of SiC and Silicon(Si)	10
2.2	Pulsed laser deposition parameters [5]	13
4.1	Experimental conditions for SiC thin films grown on Si substrate for a total duration 3 hours. *: represents the sample deposited on full wafer.	30
4.2	Thickness of samples deposited at different conditions *: represents the sample deposited on full wafer	31
4.3	Results Summary for sample 7,13, and 14, deposited at 300 °C, 600 °C, 950 °C, respectively	41

Chapter 1

Introduction

1.1 Theory of Thermal Transport in Crystalline Materials

Thermal energy is transported, in solid materials, by electrons and lattice vibration. The electrons usually dominate thermal transport in metals, whereas in semiconductors and insulators, lattice vibrations dominate. For crystals, in the harmonic limit, the solutions of equations of motion are plane wave modulated vibrations, where the summation of the solutions with similar wave vectors together will lead to a wave packet that propagates at a certain velocity. The quantization of collective atomic vibrational energy is called a phonon, which has its own wave vector. The thermal energy carried by the phonon is correspondent to particles traveling in the crystals. Where the ensembles of phonon modes with same frequency, named phonon wave-packets, can travel along distance before they can scatter by impurities, grain boundaries or other phonons. The scattering of phonons with each other results in resistance, resembling the transport gas molecules, hence, thermal transport in periodic solids is treated as the diffusion of phonons due to temperature gradient inside the crystal. This theory is well known as the "phonon gas model". The thermal conductivity (κ) contributed by phonons is determined by the energy carried by each phonon (wave packet), the group velocity of the phonons (v_g), and the average distance (l) a phonon travel between two successive scattering event, known as the phonon Mean Free Path (MFP). Based on the kinetic theory of gases and Debye's specific heat theory, the thermal conductivity of a crystalline solid can be expressed as [6]:

$$\kappa = \frac{1}{3}C_V v_g l = \frac{1}{3}C_v v_g^2 \tau \quad (1.1)$$

where C_V is the specific heat per unit volume, and τ is the relaxation time. Perierls extended specific heat theory and Boltzmann's equation for the kinetic theory of gasses.[7, 8] He proposed that phonons obey Bose-Einstein statistical

distribution, and the phonon distribution gives the heat flux, and can be obtained by solving the Peierls-Boltzmann transport equation. Peierl's theory noted that at low temperature, the lattice thermal conductivity increases with the increasing temperature because of the dependence of specific heat on temperature. While, at high temperature, the lattice thermal conductivity decreases with increasing temperature due to increased scattering rate.

1.2 Theory of Thermal Transport in Amorphous-ness Materials

Amorphous material lacks the translational symmetry and periodicity over long distance found in crystals. Thus the concepts of phonon dispersion relations, phonon group velocity, or MFP are not well defined, this posing a huge challenge for modeling thermal transport in amorphous materials. In 1911, the first theoretical model on heat conduction in amorphous materials was proposed by Einstein, introducing the "amorphous limit" model.[9] While assuming that, in solid materials, the vibrations of each atom are independent and unrelated and their frequencies are the same, named the Einstein frequency. In this model, "random walk" of these independent oscillator describes heat conduction. In 1979, Slack refined the "amorphous limit" model by equating the minimum MFP with the wavelength of phonons namely $l=\lambda$. The thermal conductivity from this model is known as the "minimum thermal conductivity" κ_{min} . [10] However, strong interactions take place between atoms in solid materials, and an atom cannot independently vibrate without affecting adjacent atoms. In addition, the frequencies of atomic vibrations are different. Hence in 1992, Cahill et al.[1] further modified the "minimum thermal conductivity" model, introducing series of oscillators with the MFPs of these oscillators being half the Debye wavelength, and the frequencies of the oscillators are given by the low frequency speed of sound $\omega=2\pi v/\lambda$. The lattice thermal conductivity can be formulated as

$$\kappa_{min} = \left(\frac{\pi}{6}\right)^{\frac{1}{3}} k_B n^{\frac{2}{3}} \sum_i v_i \left(\frac{T}{\Theta_D}\right)^2 \int_0^{\frac{\Theta_D}{T}} \frac{x^3 e^x}{(e^x - 1)^2} dx \quad (1.2)$$

The sum is taken over three acoustic modes, two transverse modes and one longitudinal mode, with speed of sound, v_i and the Debye temperature, Θ_D . This model worked for a large number of amorphous material. Lately, Agen et al. formulated a minimum thermal conductivity model for diffusion-mediated thermal transport named diffusion minimum thermal conductivity model.[11] They characterized κ_{diff} as the limit of the thermal conductivity when heat carriers are not propagating but also not localized.

$$\kappa_{diff} = \left(\frac{n^{\frac{1}{3}} k_B}{\pi}\right) \int_0^{\infty} \left(\frac{g(\omega)}{3n}\right) \left(\frac{h\omega}{2\pi T k_B}\right)^2 \frac{\frac{h\omega}{e^{2\pi T k_B}}}{\left(\frac{h\omega}{e^{2\pi T k_B}} - 1\right)^2} \omega d\omega \quad (1.3)$$

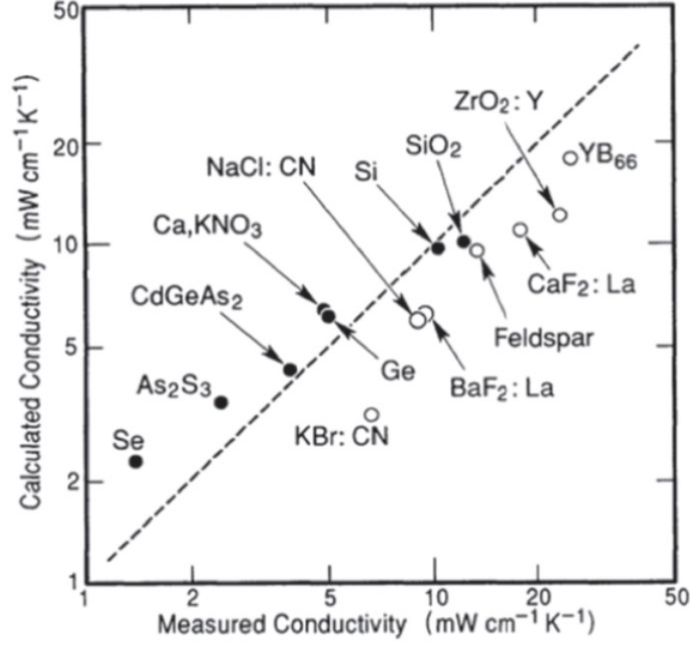


Figure 1.1: Calculated thermal conductivity (based on equation 1.2 versus measured at room temperature) [1]

where n is number density of atoms, $g(\omega)$ is the phonon density of states, which can be obtained from DFT calculations. This model usually predicts lower thermal conductivity than that of the Cahill model.

In amorphous materials, the lattice vibrational properties are different from those of the crystalline materials. In crystalline materials, the phonons describe the lattice vibrations, which are plane-wave like and delocalized. Using Debye model, which treats solid as an elastic continuum, the vibrational density of states (VDOS) of crystalline materials has a quadratic frequency dependence at low frequency, $g_D(\omega) \propto \omega^2$. From $g_D(\omega)$, one can calculate the heat capacity, which has a characteristic cubic temperature dependence, $C_V(T) \propto T^3$. However, the phonon MFP is independent of temperature. Hence, according to equation (1.1) the thermal conductivity temperature dependence is related to the heat capacity. More precisely, at low temperature, the thermal conductivity has a characteristic cubic temperature dependence, $\kappa(T) \propto T^3$. At high temperature, the heat capacity is independent of temperature following the Dulong-Petit law. However, the phonon MFP decreases inversely with temperature because to the increased strength of the Umklapp phonon-phonon scattering. Hence, the thermal conductivity temperature dependence at high temperature follow T^{-1} .

In contrast, in amorphous materials, thermal properties show significant difference than that of crystalline materials. In low temperature region, the heat

capacity of amorphous material higher than that of crystalline materials, having the Debye T^3 term and is nearly a linear dependence on temperature.

$$C_v(T) = c_1 T^{1+\beta} + c_2 T^3 \quad (1.4)$$

where c_1 and c_2 are constants and depending on the material β ranges from 0.1 to 0.3. Hence, at temperatures lower than 1K, the heat capacity follows a nearly linear dependence on temperature, instead than the Debye T^3 law. Moreover, the

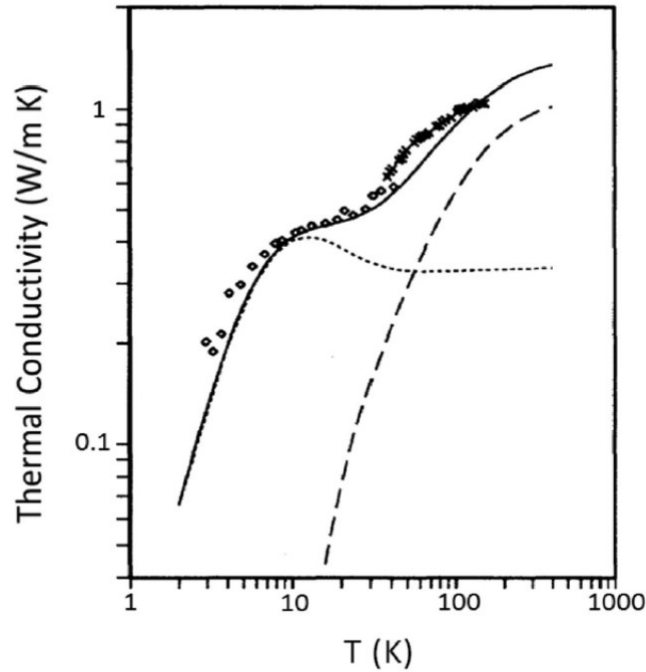


Figure 1.2: Thermal conductivity versus temperature in amorphous Silicon [2]

thermal conductivity in amorphous material has a unique characteristic, compared to that of crystalline, is different temperature dependence. The thermal conductivity of amorphous materials increases with the increase of temperature. For example, the thermal conductivity of amorphous silicon, as show in Figure 1.2, is categorized into three regimes. The first at $T < T_1$ ($T_1 \approx 10K$), the thermal conductivity is roughly a quadratic function of temperature, which is explained by the two-level scattering model. The second at temperatures $T_1 < T < T_2$ ($T_2 \approx 30 K$), a thermal conductivity "plateau" arise. The third at temperatures higher than T_2 , the thermal conductivity smoothly increases till it reaches a saturation value.

To explain this this phenomenon, in 1993, Allen and Feldman studied thermal transport mechanism in amorphous materials.[12] They classified the vibrational modes into three different categories: plan-wave-like propagons, diffusons, and

locons as illustrated in Figure 1.3 . Propagons are phonon-like modes, which are

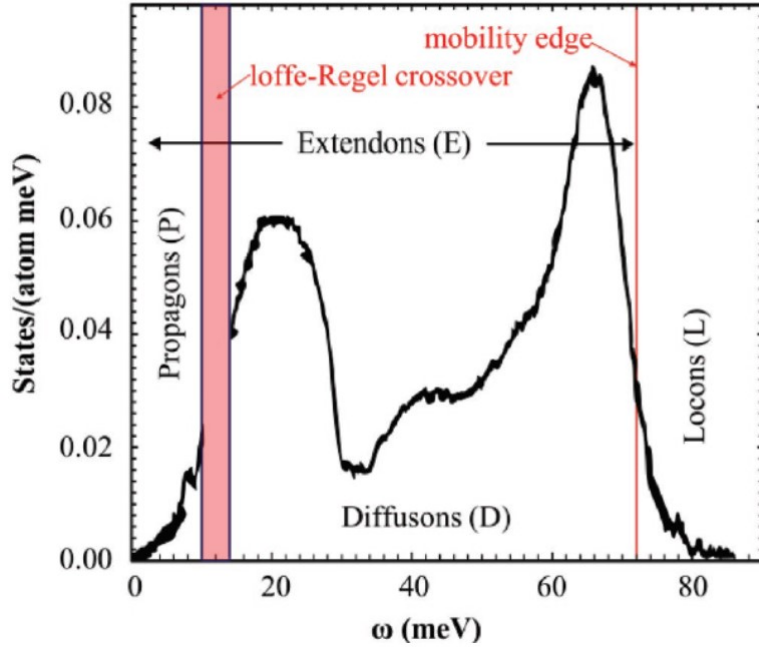


Figure 1.3: Illustration of density of vibrational states of amorphous silicon and the three types of heat carriers [3]

low-frequency delocalized vibrational modes with sinusoidal modulated velocity fields, having well defined wave vectors, and contribute to about 4% of the total number of modes. Diffusons are delocalized vibrational modes where the wave vectors cannot be defined, and contribute to about 93% of the total number of modes. Even though propagons are heat carriers exhibited in amorphous solids, their eigenvectors have a certain periodicity. While the eigenvectors of diffusons appear to be random and exhibiting no periodicity. Hence for diffusons, heat is transported through a diffusive process instead of propagating from one location to the next. On the contrary, the locons corresponds to localized vibrations, and contribute about 3% of the total number of modes. The boundary between Propagons and diffusons was named "Ioffe-Regel (IR) limit" by Mott or the "Ioffe-Regel crossover" by Allen et al.[3]. The boundary between diffusons and locons is named the "mobility edge". The contribution of diffusons dominate in heat transport due to their significant proportion, even though their MFPs are short. Propagons have a non-negligible contribution to heat transport due to their long MFPs. While locons contribution to heat transport is negligible since they are totally local and non-propagating.

Allen and Feldman proposed the following equation for calculating the diffu-

sion contribution to the thermal conductivity

$$\kappa = \frac{1}{V} \sum_i C_i \cdot D_i \quad (1.5)$$

where V is the system volume, i is the mode index, D_i is the diffusivity, and C_i is the specific heat for the related modes.

This model successfully explains the experimental results. The solid lines in Figure 1.2 shows that the thermal conductivity of amorphous silicon is contributed by two different channels. The first is heat carried by propagons, which dominates at low temperatures below the "plateau" region. Propagons are scattered by special inelastic processes, like phonons, causing a peak at $T \approx 20$ K, which becomes the plateau. The second is heat contributed by diffusons, which are non-propagating because of the absence of periodicity but mostly not localized. The contribution from diffusons is also named the "minimum thermal conductivity", which resembles the specific heat and saturates to a constant value at high temperature. The addition of these two terms creates the experimentally reported "plateau" on the thermal conductivity of amorphous silicon seen in Figure 1.2.[13, 14]

Chapter 2

An Overview of Silicon Carbide & Pulsed Laser Deposition

2.1 Silicon Carbide definition

Semiconductor power devices have played an essential role in many applications, such as military applications, and microwave communications, where high electric performance is needed. Silicon-based devices fail to meet the characteristics of high-performance power devices, such as a high on/off current ratio, high breakdown voltage, fast switching speed, excellent performance under high temperature, low leakage current, and many other characteristics. Hence, researchers have continuously worked on materials with better performance and properties. Crystalline Silicon carbide (c-SiC), one of the wide bandgap (WBG) material, has the potential to substitute silicon in high power devices. [15] The development of SiC-based devices that can function under extreme conditions will assist multiple technological fields ranging from aerospace industry, to power delivery systems, microwave communications and microelectronic mechanical systems (MEMS). [16]

SiC is a wide band semiconductor consisting of group IV silicon (Si) and carbon (C) tetrahedrally bonded together in a 1:1 ratio as shown in Figure 2.1. The distance, marked as 'a' in Figure 2.1, between neighboring Si or C atoms is approximately 3.08 Å, whereas for "C-Si" this distance is approximately 1.89 Å.

SiC carbide exists in multiple crystal structures called polytypes. However, the structure of all these polytypes can be divided into three main categories, cubic (C), hexagonal (H), and rhombohedral (R).

All known polytypes of SiC crystallize according to the laws of close spherical packing which lead them to have binary structure of identical layers. In figure 2.2, the stacking of the centers of the spheres next to each other making a layer of SiC can be seen. The center of the atoms in the first layer are all on point A while in the second layer the center of the atoms is shifted toward the voids of the first

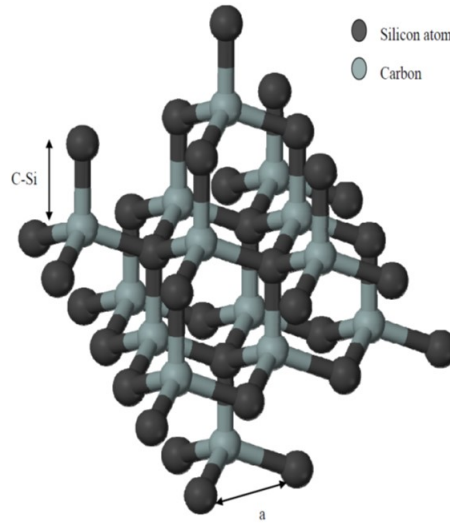


Figure 2.1: SiC Tetragonal bonding of a Carbon atom with the four nearest Silicon neighbors

layer to the points B or C. If the center's of the second layer are at point B then the layer after that can be at points A or C. if they are on point C then the layer after that can be on point B or A. Referring to the possible positions as A, B, and C, the different polytypes can be built by organizing the repetitive stacking sequence, as AB, ABC, ABAB. Polytypes are usually characterized by Ramsdell designations, a natural number before the letter symbol characterizing the crystal. This number is equal to the number of bilayers in periodic sequence. [17] The

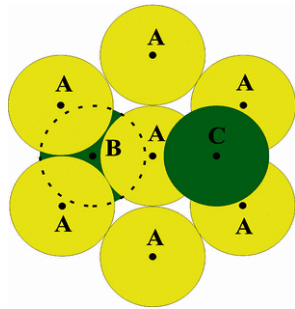


Figure 2.2: Schematic positions of atom centers for a close spherical packing. There are only three possible positions for atom centers—A, B and C [4]

cubic structure, also known as β -SiC, consists of one polytype 3C-SiC. The hexagonal and rhombohedral classes of SiC polytypes are collectively known as α -SiC. For the hexagonal class, there are several polytypes such as 2H-SiC, 4H-SiC and 6H-SiC, whereas the rhombohedral which is the least common polytype has several types 15R-SiC, 21R-SiC and 33R-SiC. Among 200 SiC known polytypes,

the commonly used for electronic devices are 3C-SiC, 4H-SiC, and 6H-SiC. Figure 2.3 shows the stacking sequence of the most four common polytypes.

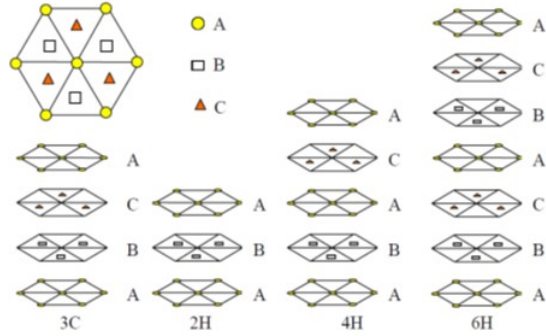


Figure 2.3: The stacking Sequence of Most Common SiC Polytypes [4]

On the other hand, amorphous SiC (a-SiC) has growing applications for optoelectronic devices, protective coating, and membrane material for X-ray lithography. The main reason for the interest in a-SiC is the combination of optical and electronic properties and excellent mechanical characteristics. Its hardness value is exceeding 50 GPa. Additionally, the optical and electrical properties of a-SiC can be controlled by changing the bonding configuration. All of that makes a-SiC suitable for the fabrication of LEDs, high-speed bipolar transistors, microwave power transistors, and sensors.

2.2 Silicon Carbide unique properties

Silicon Carbide has several unique properties, making it a highly technologically attractive material.

Table 2.1 compares some of the important properties of the most common polytypes with Silicon(Si).

2.2.1 Mechanical properties

First, SiC is the most stable carbide at high temperatures in air. Second it preserves its strength at high temperatures. Third, it is one of the hardest materials. [18] Theoretically the density of SiC is 3.21 g/cm^3 . Silicon carbide is considered as one of the hardest materials after diamond, boron carbide and cubic boron nitride. It is not only known for its high hardness but also high compressive strength, and high elastic moduli. The strong covalent bonds between silicon and carbon are what bring about such high values for these properties.

2.2.2 Electric properties

SiC is considered as wide bandgap material that ranges from 2.36 eV for 3C-SiC to 3.23 eV for 4H-SiC. These values are two times that of Silicon, which allows the functioning of SiC at much higher temperatures than Silicon.

SiC has a high break down electric field withstanding voltage gradient up to 1.5 - 3 MV cm⁻¹, which is 5 times larger than that of Silicon. This property is suitable for fabricating very high voltage, high power, high power-microwave devices. [19]

The conduction of SiC can be managed by impurity level, as by doping with nitrogen (N), Phosphors (P), Aluminum (Al), and boron (B) it can be increased. The conduction can be p- or n-type according to what impurity is being doped. The resistivity of SiC makes it useful as a resistor. But also the resistivity can vary depending on the impurities level. [18]

Property	Silicon(Si)	4H-SiC	6H-SiC	3C-SiC
Bandgap (eV)	1.12	3.23	3	2.36
Breakdown field strength (MV cm ⁻¹)	0.3	3.5	3.5	>1
Electron mobility at N _D =10 ¹⁶ cm ⁻³ (cm ² V ⁻¹ s ⁻¹)	1200	800	60 or 400	750
Saturated electron drift velocity(10 ⁷ cm s ⁻¹)	1	2	2	2.5
Thermal conductivity (W cm ⁻¹ K ⁻¹)	1.5	3.7	3.6	3.2
Thermal diffusivity (cm ⁻² s ⁻¹)	0.88	1.7	2.2	1.6
Young's Modulus (G Pa)	190	347	347	314
Density(g cm ⁻¹)	2.3	3.2	3.2	3.2

Table 2.1: Comparison of the properties of SiC and Silicon(Si)

2.2.3 Thermal properties

The SiC is known for its low thermal expansion, and the high thermal conductivity expanding its application. The excellent thermal conductivity enables the heat to flow much better than other semiconductors. In fact, the thermal conductivity of SiC exceeds that of metal at RT. This extreme property helps in manufacturing very high-power devices from SiC. [18, 19]

2.3 Pulsed Laser Deposition

2.3.1 Mechanism of PLD Process

We used Pulsed Laser Deposition (PLD) to deposit Silicon Carbide thin films on Silicon. This technique was established and popularized in 1087 due to its

success in growing superconductor thin film by Dijkkamp and coworkers.[20], and is currently being used to grow a variety of materials.

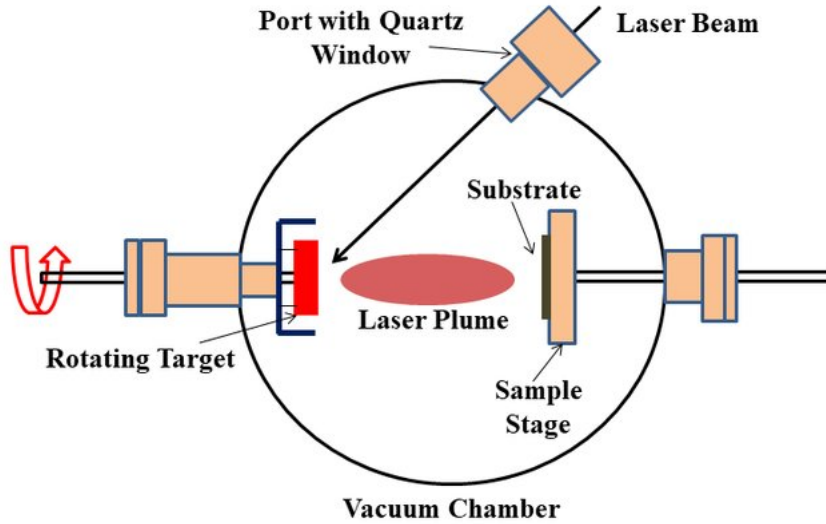


Figure 2.4: Schematic of PLD technique

A schematic of PLD is shown in Figure 2.4. The absorbed energy density from the laser pulses is sufficient to ablate material from the target creating hot plasma (plume). The plume will expand in the chamber toward the substrate, where it re-condenses to form the thin film after some hundreds or thousands of pulses.[21]

Several experimental parameters influence the growth and the quality of the films, including the substrate temperature, laser-pulse energy density, repetition rate, the distance between target and substrate, and background gas in the chamber. One of the essential ablation parameters is the laser-pulse energy density, or fluence. Therefore, when the fluence is sufficiently high, rapid evaporation of the material happens, which ensures that all the target components evaporate at the same time, achieving stoichiometry transfer of the material from the target.[21] The amount of deposited material per surface area unit also depends on the target-to-substrate distance, if the distance is greater than less material is deposited. The PLD can be carried out in vacuum or different gas pressures. At vacuum, the extracted particles have high kinetic energy that might cause localized damages and sputtering during growth. A background gas (inert gas), e.g., argon gas, can be utilized to reduce the kinetic energy of the plume, which is accompanied by changes in texture and lowering resputtering effects.[20] Therefore, deposition of metal oxides is usually carried out in the presence of oxygen gas to ensure enough oxygen is bonded to the metals. On the other hand, nitrides should be carried out in the presence of nitrogen gas. Another, the main parameter that influences the crystallinity of films is substrate temperature.

2.3.2 Advantages and Disadvantages of PLD

There are several advantages to use PLD as a film growth technique:

1. The ability to ablate almost any material due to the flexibility of laser-related parameters as wavelength, repetition rate, power density.
2. Stoichiometry transfer can be obtained for most material or material combination.
3. Multilayered material can be deposited using a multi-target holder.
4. Thin film properties can be carefully controlled through a proper understanding of the process.

Nevertheless, there are some disadvantages to perform PLD:

1. Particulates can reach the substrate, causing changes in the properties of grown films.
2. Narrow angular distribution of plume causes a lack of uniformity over large areas.

The particulates problem can be solved by polishing the target and by using a high-velocity pass filter, a mechanical filter that consists of a velocity selector, whereas the second problem can be solved by rastering the laser spot across the target or rotating the substrate during deposition. [21, 22, 23]

2.4 PLD growth of SiC

There is multiple growth techniques for single crystalline SiC such as Chemical Vapor Deposition (CVD), Molecular Beam Epitaxy (MBE) and plasma or laser CVD. PLD is an alternative growth technique for SiC with lower substrate temperature than other techniques, high deposition rate and producing relatively stoichiometric films.[5] The first recorded work of synthesizing SiC using laser ablation was in 1990.[24, 25] Balooch et al. concentrated on determining the chemical composition and surface morphology of the films, also reported the growth of poly-crystalline β -SiC films on Si using an excimer laser and Si substrate at a temperature of 800 °C.[24] During the same year, Chen and Murray achieved the crystallinity of SiC films at 500 and 900 °C substrate temperature using Nd:YAG laser. They also reported that the temperature of the substrate affects the properties of the SiC thin film.[25]

The first successful deposition at room temperature using KrF excimer was in 1994. The deposited SiC was amorphous but contained some crystallinity of β -SiC, due to molten particulate emitted from the 6H-SiC target.[26] Rimai et al.

performed the first systematic study of the PLD of SiC on transparent insulating substrates such as fused quartz, silica, and R-cut sapphire at 14 temperatures varying from 300 to 1150 °C. The structure of the SiC thin films depended on the substrate temperature. The films deposited at a temperature above 850 °C were crystalline, while films deposited at a temperature lower than 600 °C were amorphous.[27] All films deposited between 400°C and 800°C were smooth with

Deposited Film	Laser	λ (nm)	τ (ns)	Repetition Rate (Hz)	Pulse Energy(mJ)	Energy Density(J cm-2)	Substrate Temperature
4H-SiC	XeCl	308	23	-	-	-	850°C
3C-SiC	ArF	193	17	3	150-200	-	800°C
6H-SiC	ArF	266	17	-	-	-	1100°C
3C-SiC	KrF	248	25	5,10	-	2.5	700°C
3C-SiC	XeCl	308	20	1	520	-	800°C
3C-SiC	KrF	248	20	10	-	5	370°C
3C-SiC	KrF	248	20	10	-	3.2	400-950°C

Table 2.2: Pulsed laser deposition parameters [5]

similar smoothness about 0.4 ± 0.8 nm. While all films deposited above 850°C are significantly rougher, and roughness sharply increases for 4.7 ± 0.8 nm for films deposited above 950°C. The roughening of the films is attributed to the formation of crystallinity.[16] Interestingly, in 1998, Soto et al. found out that the deposition of SiC films presences of argon gave better stoichiometry than SiC films grown under nitrogen or vacuum conditions.[28] Table 2.2 shows an overview of the various conditions of growing SiC using PLD.

Chapter 3

Experimental Techniques

3.1 PLD Experimental Setup

The PLD system that was used in this work is shown in figure 3.1. The system consists of a high vacuum chamber that can be pumped down to 10^{-7} mbarr using a turbo molecular backed by diaphragm pumps. The chamber consists of a target manipulator and a substrate holder. The target manipulator can hold up to four different targets and is installed on a rotary drives to allow its rotation and toggling. While the substrate holder is placed on the top of the chamber, directly above the target, with a shutter and a heater that can reach up to 950 °C ,which is measured using a thermocouple integrated in the substrate holder.

The Laser used is a KrF excimer laser operating at 248 nm wavelength and 20 ns pulsed duration is applied. Abeam-line consisting of two UV mirrors and a 45 cm focal length lens guides and focuses the laser on the target. The focused beam enters the high vacuum chamber through a UV transparent window to impinge at an angle of 45 ° on the target. The films were deposited at a fixed target-substrate distance 5cm, and for 3 hours disposition time. The detailed conditions for deposition are shown in Table 4.1.

3.2 Characterization Techniques and Analysis of Thin Films

3.2.1 Scanning Electron Microscopy (SEM)

The Scanning Electron Microscopy (SEM) is a technique that creates magnified images which shows microscopic-scale information on the size, shape, composition, crystallography and other physical and chemical properties of specimens. The basic operating principle of the SEM involves focusing an electron beam from an electron gun on the specimen by a condenser lenses. The area that is covered

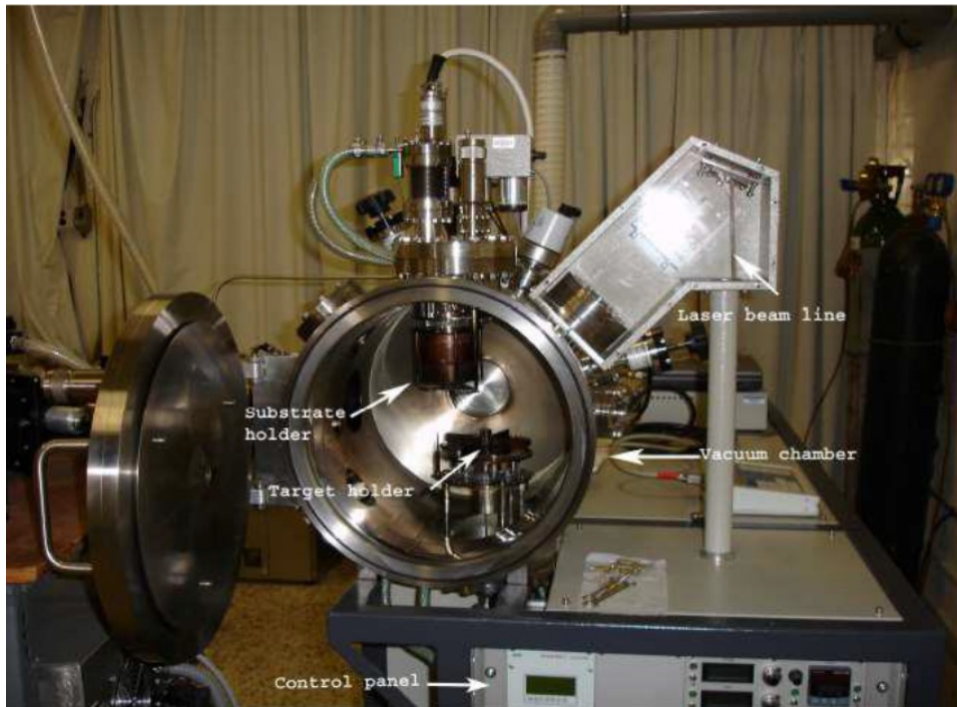


Figure 3.1: PLD Setup

by the focused by the beam can be between 10-20 nm diameter. Below the condenser lenses there are a set of scanning coils that deflects the electron beams to allow the scan of the surface, residing at each point for few microseconds. The interaction of the electron beam with the specimen produces several types of signals. The back scattered electrons (BSEs) and the secondary electrons (SEs), captured by the detector, are mainly responsible about the topographic images. Each electron is converted into a light flash by the detector then into electric pulses. These signals are amplified by a signal amplifier and utilized to modulate the brightness of each spot in a two or a three dimensional picture which is displayed on a cathode ray tube (CRT). Thus, each spot on the CRT represents a spot on the surface of the sample. The brightness of a certain spots in a SEM image is a measure of the intensity of the secondary electrons detected. The surface areas directly facing the detector will appear bright, while holes and cavities will be pictured as dark areas. All this process should take place in chamber under high vacuum ($<10\text{m}^{-4}$ Pa) to reduce unwanted scattering for beam electrons and BSEs and SEs.[29]

The MIRA 3 series scanning electron microscope was used for imaging the surface of our SiC thin films. It is available at the CRSL, and fully PC-controlled scanning electron microscopes equipped with a Schottky Field Emission (FE) electron gun made for high vacuum or variable pressure operation.

The SiC samples were installed in the SEM chamber that is pumped to a

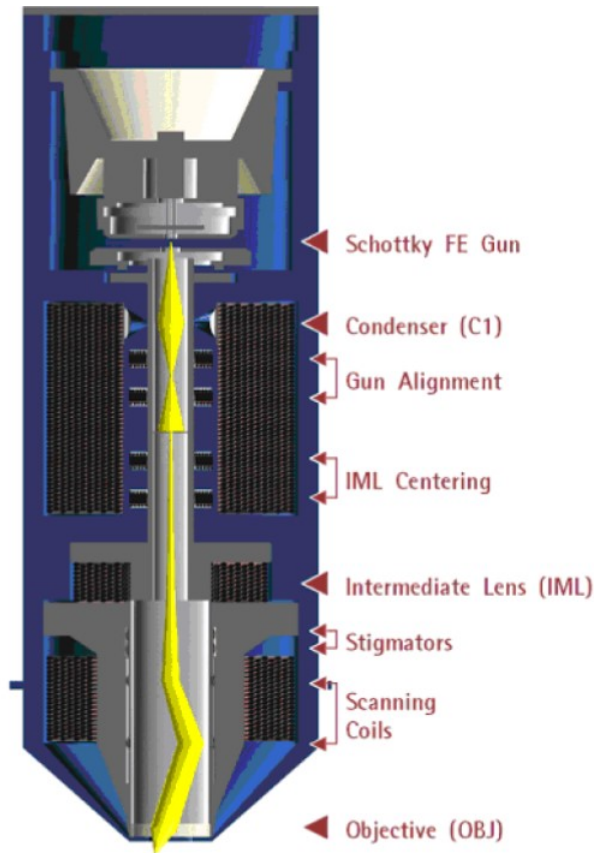


Figure 3.2: Cross section representation of the optical elements of the SEM

pressure of 0.005 Pa. The high voltage was set at 5 KV, which is the electrons' accelerating voltage between the cathode (electron gun) and the anode (thin film). To take Topographic images for the samples we choose the basic SE (secondary electron) detector and the resolution mode. Then, for getting a clear image the magnification and the working distance (WD), the distance where the electron beam focuses, were adjusted, after lowering the Z position of the sample stage (WD & Z) to 5 mm. For high magnification images the manual column centering is chosen, where the image starts wobbling, then a clear image is achieved by manually minimizing the movement of image using trackball on the Pad panel.

3.2.2 Energy-Dispersive X-Ray Spectroscopy (EDX)

The SEM is usually coupled with X-ray energy micro analyzer, where it is possible to determine the chemical composition of the sample. This technique depends on making use of the X-rays, whose specific energies provide a fingerprint that is specific to each element. Those X-rays are emitted after the interaction of the electron beam with the sample.

The INAC energy system was used to investigate the element composition of our samples. It is important to set the working distance (WD & Z) of the SEM at 15 mm and to turn off the LED in the SEM chamber before turning the INCA software so our sample is not damaged.

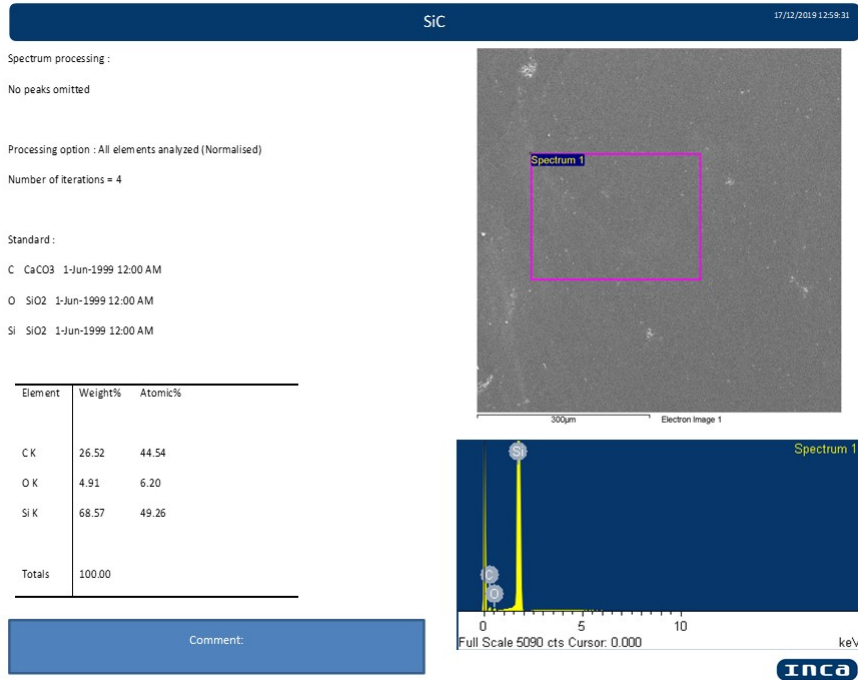


Figure 3.3: Elemental composition report by INCA of one of SiC samples (sample 8)

The figure 3.3 shows the report provided by EDX for our SiC sample. It is important to note that through using this technique it is possible to analyze a specific surface, also by increasing the high voltage (HV:10-15 KV) will allow electrons to penetrate deeper into the sample providing the element composition of deeper layers.[29]

3.2.3 Raman Spectroscopy

Theoretical Aspects

The Raman is used to determine information about the structure and properties of molecules from their vibration transitions. It was discovered by the two scientist C.V. Raman and K.S. Krishnan has discovered in 1928. [30]

The Raman Scattering is an inelastic scattering that depends on the change in rotational or vibrational quantum states of the molecules incident radiation. In a Raman experiment both elastic and inelastic scattering by the sample are

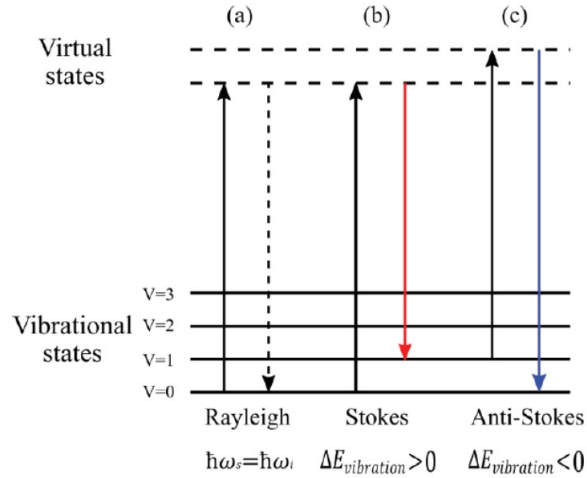


Figure 3.4: Rayleigh & Raman scattering (a) Rayleigh scattering (b) Stokes Raman scattering (scattered photon has less energy than the incident photon) and (c) anti-Stokes Raman scattering (scattered photon has more energy than the incident photon).

observed. When a light strikes a sample mostly the scattering that takes place is Rayleigh scattering (elastic scattering) with no change of photon frequency ($\hbar\omega_s = \hbar\omega_i$). However, only small fraction of the light undergoes inelastic scattering (Raman scattering). When Raman scattering happens, the excited crystal relaxes to a different vibrational level, instead of the initial state. In a Raman spectrum, the frequency shift between the scattered light $\hbar\omega_s$ and the incident light frequency $\hbar\omega_i$, represents the energy difference between the incident and the scattered light. Thus, the two frequencies are related to the vibrational energy by the following equation:

$$\hbar\omega_i = \hbar\omega_s + \Delta E_{vibration} \quad (3.1)$$

The final vibrational state of the crystal can be either higher or lower in energy than the original state. When the final vibrational state is higher than the initial state in energy, the scattered photon will exhibit a lower frequency than the incident radiation. Thus, a red shift from the excitation frequency is observed, where this type of Raman bands is referred to as Stokes Raman Scattering ($\Delta E_{vibration} > 0$). while a blue shift is observed when the final state is lower than the initial state. these Raman bands are referred to as anti-stoker Raman scattering ($\Delta E_{vibration} < 0$). Since at room temperature, most of the molecules are at the ground vibrational stat ($\nu=0$), the Stokes scattering exhibit higher Raman intensity than the anti-Stokes scattering, that originate from an excited vibrational

state, for example $\nu=1$. Thus, the Raman scattering photons that are more commonly collected and analyzed are the Stokes photons, referred to as Stokes lines. A Raman spectrum is presented as an intensity-versus-wavelength shift. Where it features a number of characterization data on the sample studied. The first component of the Raman spectrum is the characteristic Raman frequencies. Which are unique to the bonding between elements in specific material and give an idea of the composition of the material being studied. Raman can be utilized for both qualitative as well as quantitative purpose. Typically analyzing the characteristic frequencies is a qualitative manner. Frequently one is looking for the phase information, local composition of the material, or any illegitimate peaks that indicate the presence of an unwanted component. While, the quantitative aspects of Raman can be performed by measuring the intensity of scattered radiations. The characteristic peak has a specific wave number, or Raman shift, where changes in this peak position shows stress or strain states within the sample.

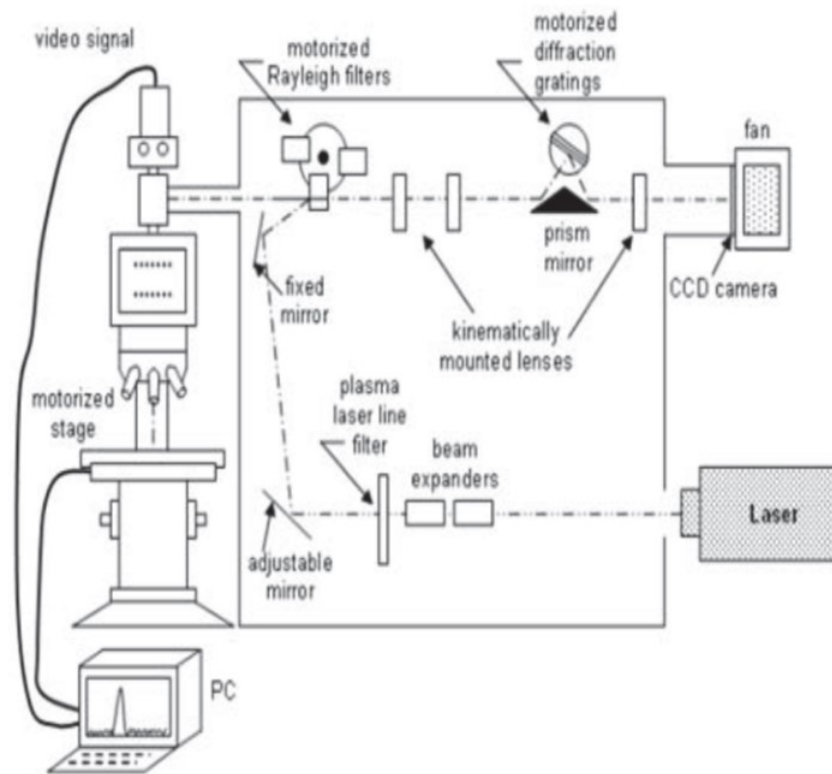


Figure 3.5: Raman spectroscopy instrumentation diagram

Moreover, the Raman peaks can show the quality of the crystal being analyzed. As wider peaks indicates disruption in order such as amorphization, or some other plastic deformation within the sample. Also the peak intensities are related

to the amount of the material that is being studied. Whereas the larger characteristic peaks of the substrate the thinner the deposited film is. since thicker films mean less chance of the scattered photons from the substrate reaching the detector. Thus it can be also an indication of the amount of material in the film, due to relative intensities between the peaks.[31]

Instrumentation

The Raman instrumentation, shown in Figure 3.5 was used to study the crystallinity of our SiC samples. It is consisted of the following main constituents, an excitation source, a light detector and a light collection and delivery system. The excitation source consists of a laser, which is detected using a Charged Couple Device (CCD), and an optical microscope for light collection. A Laser of a appropriate power, wavelength and constancy illuminates the sample. The exciting laser is guided to the sample using a traditional optical system of mirrors and lenses that focuses the exciting laser onto the sample and collects the resulting Raman scattered light. A sensitive, low noise, detector is used to identify the Raman scattered light. Spectral analysis is preformed on the collected data.

1. Light source: A standard Raman laser, having a narrow line width which is around 1 to 10 cm^{-1} , lower power consumption, a stable power output and a stable wavelength output. The power used in Raman spectroscopy for the excitation laser is in the range of 3-10 mWs. It also requires a monochromatic light source to keep a good spectral resolution.
2. Light Detector: It is a system composed of a slit, a diffraction grating, a mirror and a detector.
3. A CCD camera equipped with a cooling system.
4. Rayleigh Filters: Used to prevent the elastic light to reach the spectrometer and drowning the relatively weak Raman signals.
5. Objective Lenses: It help in focusing the laser beam, also locating a specific region in a sample.

The Raman scattering measurements for our SiC sample were executed at room temperature in the back-scattering configuration. A laser of wavelength $\lambda = 532$ nm with a 400 mW maximum power was used.

3.2.4 X-Ray Diffraction

X-ray diffraction (XRD) is usually used to characterize the crystalline form of the sample and to approximate the crystalline size. XRD of crystalline material is based the principle of the elastic scattering of the X-ray by the lattice of the

sample. When a beam of monochromatic X-ray penetrates the sample and gets diffracted by the periodic lattice of the crystalline sample, according Bragg's equation.

$$n\lambda = 2d\sin\theta \quad (3.2)$$

where θ is the incidence angle, n is an integer, λ is the X-ray wavelength, d is the spacing between crystallographic planes. Thus the crystallographic information can be obtained by the diffraction pattern generated by constructive interference of the scattered X-rays.[?]

The X-ray measurement of the SiC samples were performed by Bruker's D8 advanced X-ray diffractometer. The X-ray source is a ceramic Siemens tube operating at 40KV with a current 40mA and emitting a Cu K_α radiation of wavelength $\lambda=1.5418 \text{ \AA}$. These radiations are directed onto the sample. As the detector is rotated, the intensity of the reflected X-rays is recorded. The parameters chosen for the X-ray measurements of the samples are 0.2 s as the time per step, 0.02° as the increment and 0° - 60° for the 2θ range.

3.2.5 Profilometer

A profilometer is a measuring device used to measure surface topography, as step height (film thickness), surface roughness, waviness and stress. A diamond stylus is moved vertically in contact with the sample for a specific distance and specified contact force, where it measures the deflections of the tip. The advantages of the profilometer include surface independence and resolution, it's also a direct technique that doesn't require modeling. The Deltak XT profilometer was used to measure the thickness of the deposited samples. The stylus tip radius is $12.3 \mu m$, stylus force 0.03 mg, and for scan length 0.5mm. The results are obtained as in Figure 3.6, where the zero level is the when the stylus moving on the substrate, when the stylus moves toward the deposited films the step happens.

3.2.6 Laser Flash

Theoretical Aspects

To measure the thermal properties of the fabricated thin film a sensitive photothermal technique is used. The advantages portieres of this technique, which is based on photothermal displacement spectroscopy, are:

1. The ability to detect the heat deposited on the sample by absorbed light. Which leads to a signal linear over a large rang of optical absorption coefficient, α , and sensitive to the scattering of the incident beam.
2. It terminates the need for a photodetector sensitive in the wavelength area being studied.

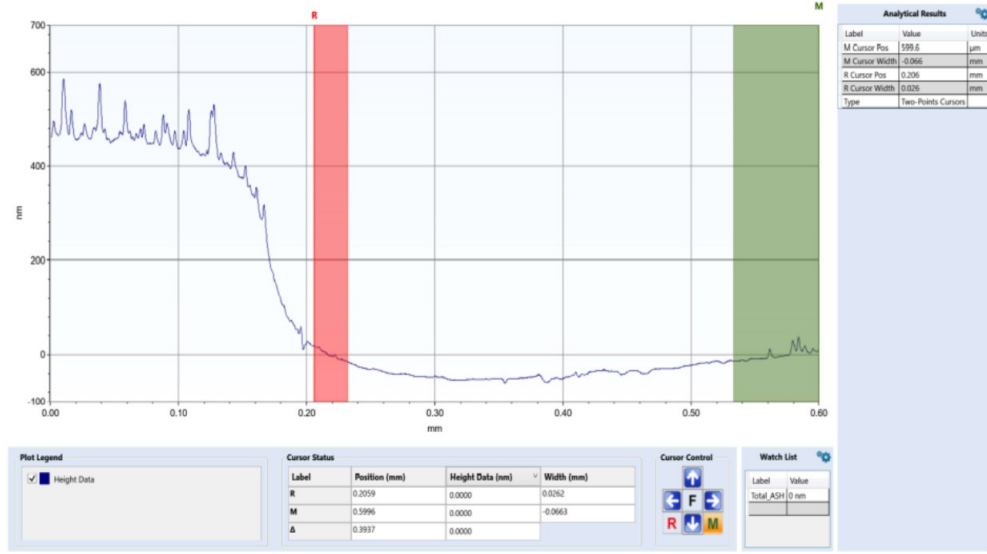


Figure 3.6: The measurement obtained by Dektak XT Profiler

3. The ability to distinguish between surface and bulk properties.
4. The lack of any electrical or mechanical contact with the sample.
5. It facilitates the study of a wide variety of materials in difficult environments.

The physical basis for photothermal displacement spectroscopy is the bending and displacement of a lighted surface due to the thermal expansion of the sample as it is heated by the absorption of electromagnetic radiation.

When the sample is heated, then optically excited electrons decay non-radiatively. the surface of the sample expands as the temperature rise, creating a bump. The displacement of the surface

$$h = \alpha_{th} T L_{eff} \quad (3.3)$$

where α_{th} is the thermal expansion coefficient, and T is the average rise in temperature over an effective length L_{eff} . The temperature rise is known as $T \propto (\text{absorbed energy/volume})/(\text{heat capacity})$. When the light is modulated at a certain frequency f, then the incident energy per cycle, of which some fraction is absorbed, is modulated to the product of power and time, or the power/2f for square wave. Hence the displacement is:

$$h = \alpha_{th} \beta P L_{eff} / (2 A L_h \pi f \rho C) \quad (3.4)$$

where β is the fraction of light absorbed, P is the incident power, A is the heated area, L_h is the heated length, ρ is mass density and C is heat capacity/g.

The inverse proportionality between displacement and frequency is valid under the condition that the thermal diffusion length of the material is much smaller than the diameter of pump beam on the sample. The thermal length is the distance over which the magnitude of planar harmonic thermal wave decays exponentially to 1/e of its initial value and its phase changes by one radian. It is written as:

$$L_{th} = \left(\frac{K_{th}}{\pi f \rho C}\right)^{1/2} = \left(\frac{\lambda}{\pi f}\right)^{1/2} \quad (3.5)$$

where K_{th} is the thermal conductivity, ρ is the mass density, C is the heat capacity/g, f is the frequency of the thermal wave, and $\lambda = K_{th}/\rho C$ is the thermal diffusivity.

On the contrary if L_{th} is greater than the pump beam diameter, it will depend on the modulation frequency yielding additional frequency dependence to the single.

An exact calculation of the surface displacement involves solving Navier-Stokes equation for a slab, under the condition that there is no normal component to the stress at the boundaries of the slab

$$(1 - 2\nu)\nabla^2 u + \nabla(\nabla \cdot u) = 2(1 + \nu)\alpha_{th}\nabla T \quad (3.6)$$

where u is the displacement vector, ν is Poisson ratio, T is the change in temperature from equilibrium value, α_{th} is the thermal expansion coefficient.

Assuming that the temperature distribution is unaffected by the expansion and is established by the expansion and is calculated using the heat equation with a source term of a Gaussian beam decaying exponentially by optical absorption

$$K_{th}\nabla^2 T - \rho C(\partial/\partial t)T = -Q(r, t) \quad (3.7)$$

where K_{th} is the thermal conductivity and

$$Q(r, t) = (P\alpha/2\pi a^2)e^{(-r^2/a^2)}e^{-\alpha z}\cos(\omega t)$$

where P is pump beam power, a is $1/e$ radius of the Gaussian pump beam, $\omega = 2\pi f$ is the angular frequency of the modulation and α is the optical absorption coefficient. Solving equations 3.6 and 3.7 gives

$$\frac{\partial u_z}{\partial r}(r, 0) = -\frac{\alpha_{th}\alpha P(1 + \rho)}{16\pi K_{th}(1 - \rho)} \left[\int_0^\infty \frac{\Delta^2 d\Delta J_1(\delta r/L)e^{-\delta^2 a^2/4l^2}}{\sinh\Delta[(\alpha L)^2] - S^2} \right. \\ \left. (R(-\alpha L) + C_1 R(-S) + C_2 R(S)) \right] \quad (3.8)$$

where

$$\bullet R(x) = \left[\frac{e^x - e^\Delta}{x - \Delta} - \frac{e^x - e^{-\Delta}}{x - \Delta} \right] + B_1 \left[\frac{e^{x+\Delta/2} - e^{-\Delta/2}}{x + \Delta} + \frac{e^{x-\Delta/2} - e^{-\Delta/2}}{x - \Delta} \right] + \\ B_2 \left[\frac{e^{x+\Delta/2} - e^{-\Delta/2}}{x + \Delta} - \frac{e^{x-\Delta/2} - e^{-\Delta/2}}{x - \Delta} \right],$$

- $C_{1,2} = (\alpha L/S)([e^{-\alpha L} - e^{\pm S}]/2\sinh(S))$,
- $B_1 = -\sinh(\Delta/2)[\Delta - (1 - 2\rho)\sinh(\Delta)]/(\Delta + \sinh(\Delta))$,
- $B_2 = \cosh(\Delta/2)(\Delta + (1 - 2\rho)\sinh(\Delta))/(\Delta - \sinh(\Delta))$,
- $S^2 = \Delta^2 + i(2L^2/L_{th}^2)$,
- L is the sample thickness
- L_{th} is the thermal length

Equation 3.8 leads to some general statements. The signal is directly proportional to the thermal expansion coefficient of the sample and to the pump beam power. The signal is linear to α when $\alpha L_{th} \ll 1$ even α appears in different places in the integral. The equation was used to plot the theoretical curves in Figure 3.7

The experimental configuration used to measure the magnitude and the phase of optically induced displacement is the Beam Deflection (BD). A pump beam is focused to the sample, and a weak probe beam is radiated to the sample and then reflected to a detector. As the pump heat intensity is modulated, the photoinduced displacement rises and falls, hence the probe beam is reflected at a different angle depending on the slope (du_z/dr) of the displacement at point (r_0) where the probe is reflected from the sample. The deflected beam is detected by a sensitive photodiode, then the output is amplified by a phase-sensitive lock in amplifier. The beam deflection signal at the detector is given as:

$$S = \gamma(2D[du_z/dr(r_0)] + 2u_z(r_0)\sin\theta + \text{smaller terms}) \quad (3.9)$$

where D is the distance from the sample to the detector, u_z is the surface displacement, θ is the angle of incidence of the probe beam and γ is the detector sensitivity [V/cm].

In equation 3.9 the first term is the deflection by slope displacement, the second is the deflection of the probe beam by vertical surface displacement, which is smaller than the first term by D/a, where a is the radius of the pump beam, which is approximately 5000. The higher order terms are because of the slight displacement of r_0 . It is advantageous to approximate that the signal is due to the first term hence it is proportional to the surface displacement and independent of incident angle of the probe beam.

The signal maps out the slope of the photoinduced displacement as the pump beam is moved across the probe beam spot of the sample. Figure 3.7 (a) shows the magnitude and Figure 3.7 (b) shows the phase versus the relative position (r_0) of the two beams. The magnitude rises as the pump beam comes near the probe beam, then goes sharply to zero with the pump beam and the probe beam overlap. When the pump beam starts to go away from the probe beam the signal then changes sign and repeat itself as a mirror image. When deviation from the

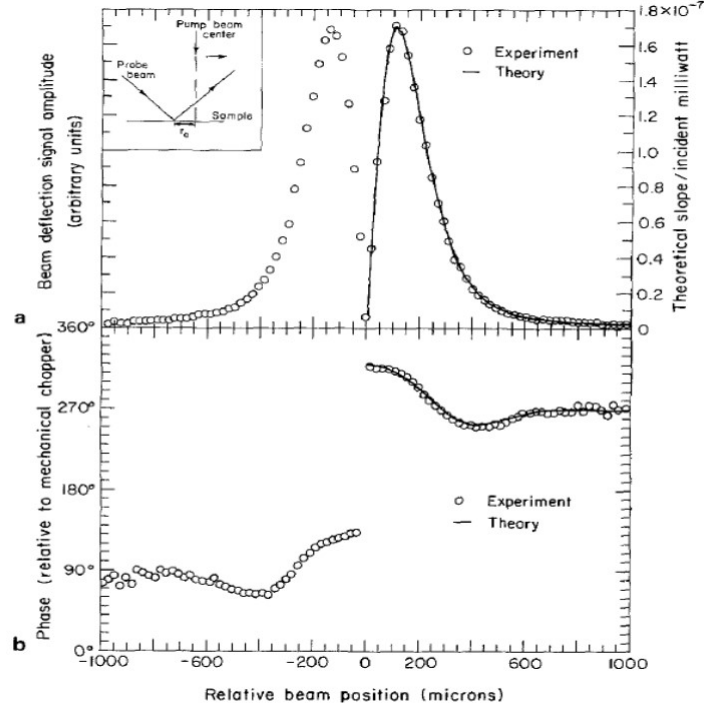


Figure 3.7: Beam Deflection (BD) signal vs. the relative position (r_0) of the pump and probe beams. The circles are experimental data of the (a) amplitude and (b) phase of the BD signal at the pump beam is translated across the sample (inset image). The solid lines are the slope magnitude and phase calculated from 3.8

mirror image is due to the alignment of the beam, as pump beam and the probe beam and the sample normal should be in the same plane. Another reason for the deviation might be the inhomogeneities, local variation in thickness. Important information is in the phase of the photothermal signal relative to the pump beam. When the pump beam is on, at first the heat is deposited where the beam meets the sample. After that the heat diffuses out from the center, and the signal starts to peak at a later time as the relative position between the probe and the pump beam starts to increase as in Figure 3.7. After a few thermal lengths the, mechanical coupling to the immediately heated area of the sample dominates, causing the phase to reach a constant value. In the case of thermal thin samples, $L < 2L_{th}$, with uniform heating and thermal thick sample with surface heat yield linear changes of the phase with the position beyond the central flat region which is approximately equal to the directly heated area. In the case of thermally and optically thin, the phase shift approximately $\frac{53^\circ}{L_{th}}$. While in the case of optically and thermal thick sample, the phase shifts approximately $\frac{27^\circ}{L_{th}}$. [32]

Experimental Setup

In order to plot the Beam Deflection signal as function of the relative position (r_0) of the pump and the probe beam the following set up was used as in Figure 3.8

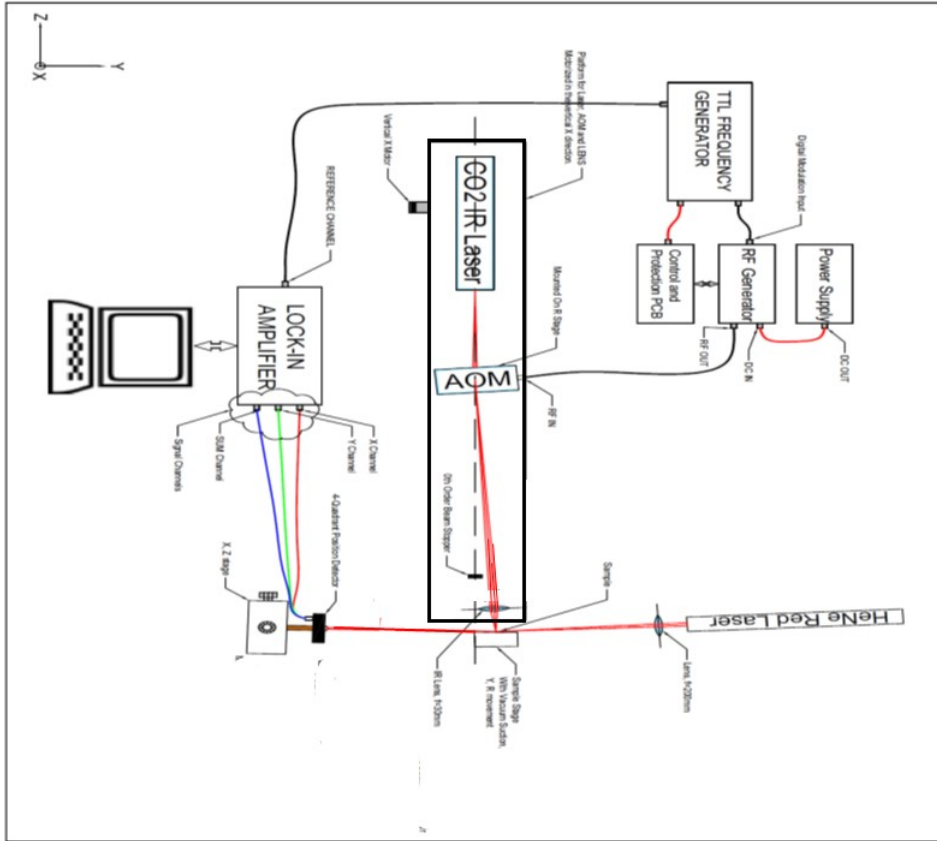


Figure 3.8: The schematic diagram of the experimental set up

The pump beam or heating beam used is a continuous CO_2 laser infrared laser, with an operating power 4 watts. Its wavelength is temperature dependent. Since the laser is continuous, the laser beam should pass through an Acousto-Optic modulator (AOM), which is used to modulate the frequency of the pump beam. The used specifications of the AOM is $16 \mu m$ wavelength, horizontal polarization, and numerical aperture up to 9.6 mm, which is enough for the pump beam. The AOM will give two diffracting beams the zeroth and the first order. The zeroth beam is modulated between 700 mW and 100 mW, the 100 mW would fix the sample heating which contradicts the theory. Hence the zeroth order beam is stopped from hitting the sample. The first order beam is modulated between 700 nW and 0 mW which is convenient for the measurement, thus the first order beam is used and maximized by the alignment. The square wave function generator is

used to control the frequency of the beam.

The pump beam is focused to the sample by an infrared lens of focal length 3cm, that focuses the beam diameter to a $71 \mu m$. Hence the sample should be precisely 3 cm away from the lens, however it is hard to specify the distance between the lens and the sample. To obtain the best results we put a paper scotch tape on the sample and we turn open the shutter of the heating laser and we check the diameter that was burned on the tape. The process is repeated by moving the sample back and forth slightly, till the best burn on the sample is obtained.

The He-Ne laser is used as a probe beam with a wavelength 632.8 nm, power 5 mW, beam diameter 0.81 mm. The probe beam is focused to the sample using a 20 cm focal length lens, thus a $100 \mu m$ probe beam is obtained on the sample.

The challenging part is to align the probe beam with the pump beam since the pump beam is infrared. Hence to do the alignment, the probe beam is aligned such that the distance between the IR spot and the probe beam is minimal on the surface of the sample.

4 Quadrant Photodetector

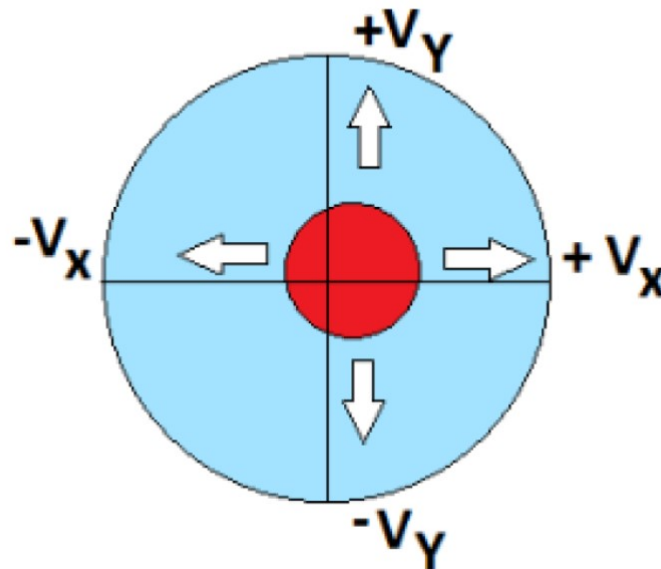


Figure 3.9: Position Sensing Quadratic Detector

The reflected probe beam from the sample is detected using the a Position Sensing Quadrant Detector, which is use to measure the deflection of the probe beam. The detector can measure both he normal and the transverse deflections as shown in the Figure 3.9. The detector operates in the wavelength rang between 400 and 1100 nm and for a spot size diameter less than 3.9 nm. The probe beam

reflection should be at the center of the detector before the shutter of the infrared laser is open.

The detector is connected to a lock-in amplifier which neglect the noise signals during the measurement.

The measurements are taken at 6 different frequency and the data are saved into an excel sheet.

Chapter 4

Results & Discussion

In this chapter, we represent the experimental results obtain in this thesis. We will start by describing the film growth conditions and follow up by the analysis of the surface morphology of the films and the accurate determination of their thickness, an important parameter when determining their thermal properties. We then present the analysis of their nano-structure and bonding properties using Raman spectroscopy and X-Ray Diffraction in order to assess which growth conditions result in amorphous or crystalline layers. Once this is determined, we report on the determination of the thermal properties of amorphous and crystalline layers using the laser flash technique, and finally we conclude with a discussion and interpretation of the obtained results.

4.1 Film Growth Conditions

Table 4.1 details the growth condition of the films grown in this work, all of which were deposited at a fixed target-substrate distance 5cm, and for a total deposition time of 3 hours. It should be noted that the last three samples in the table where growth on a full 1 inch diameter silicon wafer, whereas the others were grown on pieces of the Silicon wafer, cut in the shape of $\sim 1 \text{ cm}^2$ squares. The reason behind this was to compare if there is any difference in the growth and film properties between the two approaches, since in the first case, the Si substrate is directly heated by radiation from the Rh-Os heating resistor in the sample holder whereas in the second case, the samples where fixed to a stainless steel sample holder with a set of screws. Thus, it is important to assess if the two different approaches lead to the same or different actual values of the substrate temperature during film growth. It must also be mentioned that in some cases, a small amount of Argon gas was introduced in the chamber during growth in order to reduce film deposition on the inner side of the quartz window through which the laser beam enters the deposition chamber. The occurrence of such a deposition can eventually absorb the laser energy and thus significantly reduce

the laser energy that reaches the SiC target.

Sample	Temperature of disposition ($^{\circ}\text{C}$)	Laser Energy (mJ)	Repetition rate (Hz)	Argon Pressure (mTorr)
sample 5	300	400	10	vacuum
sample 6	300	400	10	5
sample 7	300	400	25	5
sample 8	300	400	50	5
sample 9	300	400	25	10
sample 11	25	400	25	5
sample 12	900	400	25	5
sample 13	600	400	25	5
sample 14	950*	400	25	vacuum
sample 15	700*	400	25	vacuum
sample 16	400*	400	25	vacuum

Table 4.1: Experimental conditions for SiC thin films grown on Si substrate for a total duration 3 hours.

*: represents the sample deposited on full wafer.

4.2 Thickness and Surface Morphology determination

4.2.1 Profilometer Measurements

Figure 4.1 shows the Profilometry measurements that were used to determine the thickness of several SiC films. For each sample, the thickness measurement was repeated several times at different positions of the step (which indicates the transition from substrate to film) and then averaged. The obtained thicknesses for the samples synthesized in this work are listed in Table 4.2. The first two films which were deposited under similar conditions (substrate temperature at 300 $^{\circ}\text{C}$ and a repetition rate of 10 Hz) except for the pressure have thicknesses around ~ 200 nm. This is important to note at this stage because this shows that the addition of a pressure of 5 mTorr of Ar during growth has, for all practical purposes, no effect on growth rate.

In order to elucidate the effect of laser repetition rate, one can compare samples 6, 7 and 8 which were grown at 10, 25 and 50 Hz, respectively (all other experimental conditions kept the same). From Table 4.2, it is seen that thickness increases from 210 to 600 nm when repetition rate increased from 10 to 25 Hz, an almost linear dependence. Further increase in repetition rate to 50 Hz leads

Sample	Deposition temperature (°C)	Repetition rate (Hz)	Film thickness (nm)
sample 5	300	10	198 ± 9
sample 6	300	10	210 ± 11
sample 7	300	25	602 ± 30
sample 8	300	50	407 ± 20
sample 9	300	25	173 ± 9
sample 11	25	50	440 ± 22
sample 12	900	50	493 ± 25
sample 13	600	50	470 ± 24
sample 14	950*	50	75 ± 38

Table 4.2: Thickness of samples deposited at different conditions
*: represents the sample deposited on full wafer

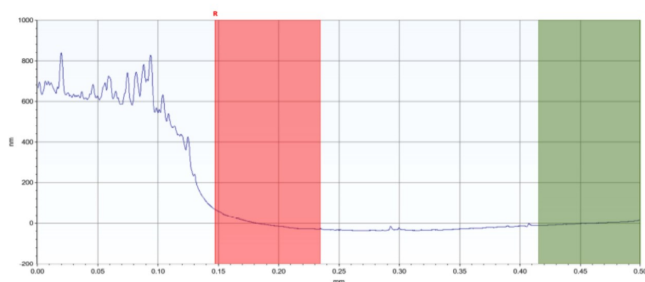
to a significant decrease in film thickness, reaching about 400 nm. This decrease would result from a rapid film deposition of SiC on the quartz window, which could block the transmission of the laser beam, thus leading to a lower film thickness than for a repetition rate of 25 Hz. From the above observations, we have opted to pursue the film deposition experiments in this thesis at a repetition rate of 25 Hz that allows a higher growth rate than 10 Hz, while avoiding drawbacks such as film deposition on the quartz window.

While fixing the repetition rate at 25 Hz and the deposition temperature at 300 C, samples 7 and 9 have been grown at 5 and 10 mTorr, leading to thicknesses of 600 and 170 nm, respectively. The sharp reduction in growth rate would result from the scattering of the ablated species in the plume because of collisions, thus resulting in lower film thicknesses. Thus, we opted to perform further deposition experiments at 5 mTorr or under vacuum conditions.

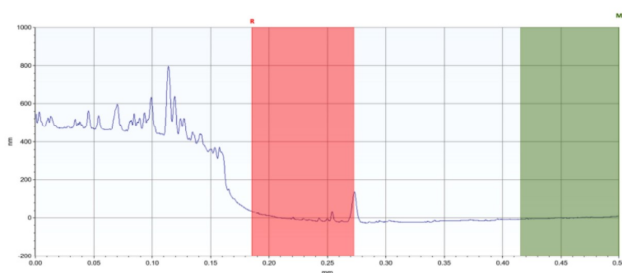
The next parameter that was investigated was the temperature. This is a crucial parameter that determines, to a large extent, the crystalline nature of the films. Thus, three samples were grown at 25, 600 and 900 °C, while keeping all other deposition conditions fixed, as described in Table 4.2. These samples, numbered 11, 13 and 12, lead to film thicknesses of 440, 490 and 470 nm, respectively. Keeping in mind an experimental uncertainty on the measurements of about 25 nm, the growth rate is weakly dependent on substrate temperature. The three remaining samples in the table are those that were deposited on the full rotating 1 inch Si substrate. The thickness measurements indicated that these films are around 75 nm. This is lower than the thickness on the fixed small area samples because the rotation spread the deposited material over a much larger area.

From these results, we undertook a nano-structural study of the effect of temperature for films grown in vacuum or at 5 mTorr, with a repetition rate

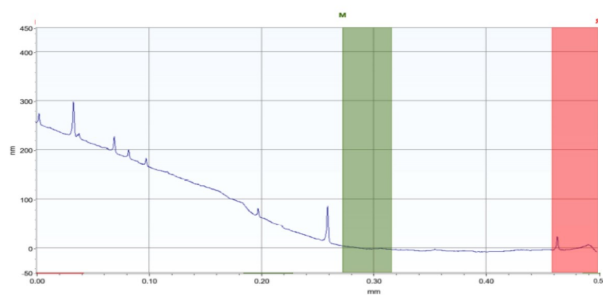
of 25 Hz, including an investigation of their thermal properties. This study is detailed in the following sections of this chapter.



(a) sample 7



(b) sample 13



(c) sample 14

Figure 4.1: Surface profilometry measurements of SiC films deposited on Si substrate (a) at 300 °C and (b) at 600 °C (c) at 950 °C

4.2.2 Scanning Electron Microscopy Imaging

Figure 4.2 shows SEM images for sample 7 and 13, which were deposited at 300 °C and 600 °C respectively. In both cases, surface of samples appear to be relatively smooth, however with the presence of some droplets. These droplets are observed for PLD grown films as a result of a possible splashing of the target during film growth, especially for high laser power density at the target. Reducing the power density could result in a reduction of droplets formation, but it could also be accompanied by a reduction in the deposition rate. On the other hand, the SEM images confirm the absence of delamination and cracks in the films, which is crucial for proper determination of their thermal properties, as will be presented later in the chapter. Unfortunately, the SEM was not accessible to perform imaging on the film grown at 950 °C in attempt to observe the formation of crystalline grains.

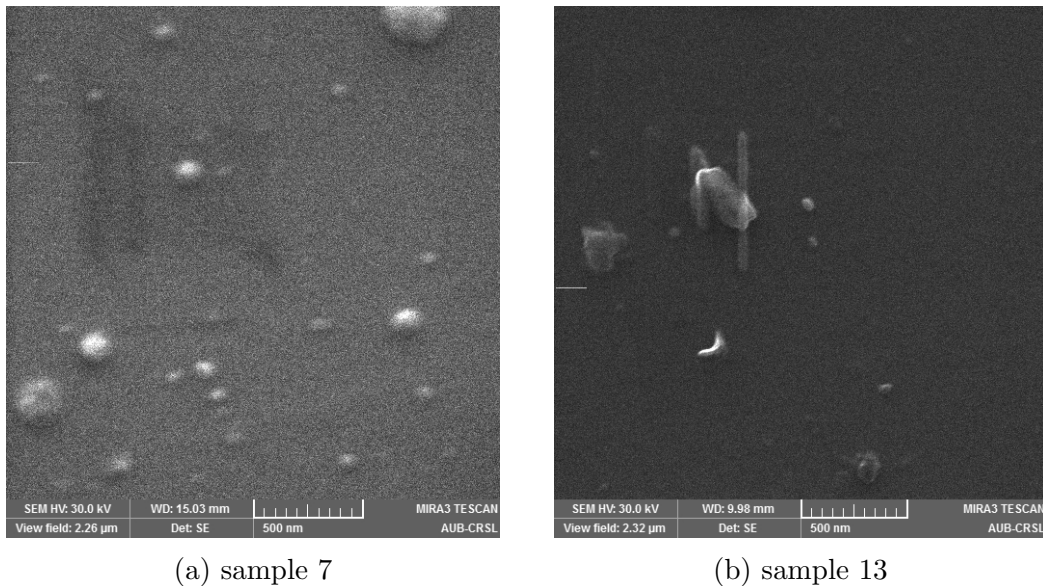


Figure 4.2: SEM Images of SiC films deposited on Si substrate (a) at 300 °C and (b) at 600 °C

4.3 Raman Spectroscopy

Three samples were selected to perform the Raman analysis, as shown in Figure 4.3. They are the films grown on Si substrate at temperatures 950 °C (sample 14), 600 °C (sample 13), and 300 °C (sample 7). All samples show effectively three apparent broad bands in regions $[300-600] \text{ cm}^{-1}$, $[700-1000] \text{ cm}^{-1}$ and $[1300-1600] \text{ cm}^{-1}$. The first band from $[300 \text{ to } 600] \text{ cm}^{-1}$ corresponds to Si-Si bonds of the Si substrate, and possibly the presence of some Si-Si bonds

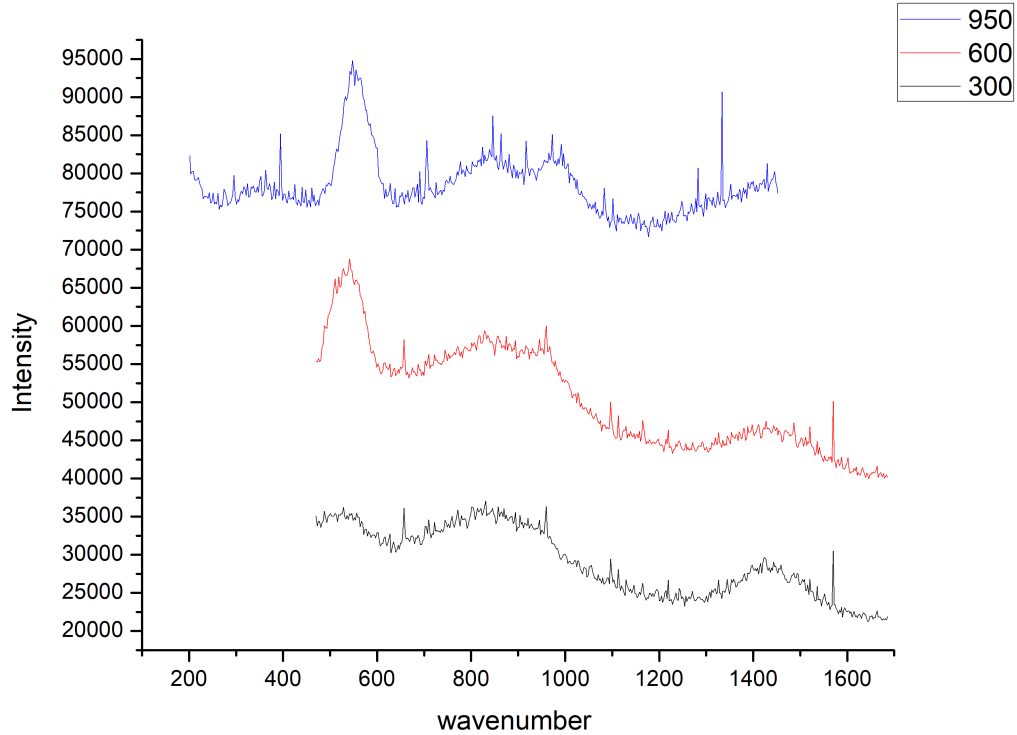


Figure 4.3: Raman spectra of SiC films deposited on Si substrate at temperatures 950 °C (sample 14), 600 °C (sample 13), and 300 °C (sample 7)

within the SiC matrix of the thin film. We notice that as the thickness of the SiC film increase the intensity of the Si-Si signature becomes smaller. Indeed, sample 14 has lowest thickness (75 nm) and shows the largest Si-Si peak whereas sample 7 has the highest thickness (600 nm) shows a barely visible Si-Si signature. The second band [1300 to 1600] cm^{-1} corresponds to the C-C bonds. Looking at the signal within this range, it is clear that it is essentially the signature of the two well know peaks, D (Disorder typically around 1350 cm^{-1}) and G (Graphitic typically around 1550 cm^{-1}) that are frequently reported for amorphous carbon samples. Careful examination of these two bands shows that the D and G bands become more resolved from each other as the deposition temperature is increased, thereby indicating less amorphization. The remaining band of interest is the one appearing between 600 and 1000 cm^{-1} where there is broad peaks is due to Si-C bonds. Since in perfect SiC cubic crystal, there is two sharp lines around 796 cm^{-1} and 972 cm^{-1} , but a-SiC has a band in the region [700-725] cm^{-1} . These two lines of the perfect crystal are attributed to the transverse optical (TO) and longitudinal optical (LO) modes of 3C-SiC, respectively. The peak of the LO mode would also overlap with second order silicon peak around 950 cm^{-1} .

The broadening of the SiC peaks is due to decrease in the crystalline size and the increase in the density of stacking faults. [33, 34] We can notice at deposition temperature 300 °C the region between [600-1000] cm^{-1} is broad with no dominate peaks showing that the sample 7 is amorphous. Then as deposition temperature increase to 600 and 900 °C the peaks around 796 cm^{-1} and 972 cm^{-1} start to increase, then the degree of crystallinity starts to increase. Hence, sample 13 and 14 are amorphous with some degree of crystallinity, as sample 14 has higher degree of crystallinity than sample 13.

4.4 X-Ray Diffraction

Figure 4.4 shows the XRD pattern for the three samples 7 (300 °C), 13 (600 °C) and 14 (950 °C). The XRD signal of sample 7 is devoid of any peak, indicating the amorphous nature of the films grown at 300 C. The other two sample show a pronounced but wide XRD peak at 34 ° which can be attributed to the formation of crystalline SiC. In literature, the XRD data for β -SiC shows peaks at 35.7 °

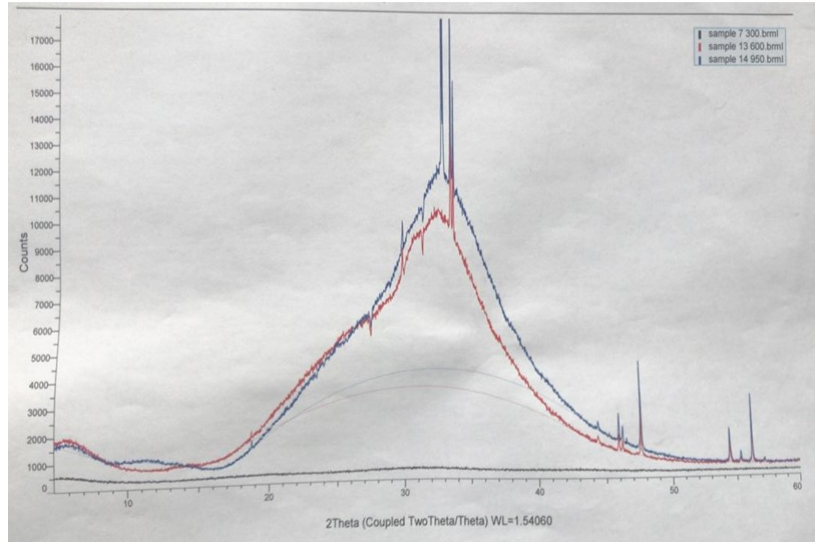


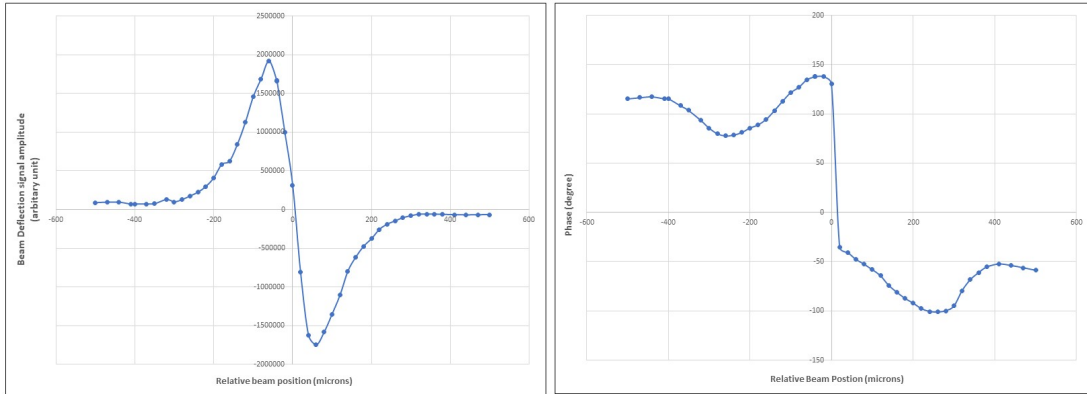
Figure 4.4: XRD pattern of SiC films deposited on Si substrate at temperatures 950 °C (sample 14), 600 °C (sample 13), and 300 °C (sample 7)

and at 33.7 °, and α -SiC shows peak at 34.1 °. The broadening observed in the patterns is due to intrinsic characteristics of the material, such as particle size, stacking fault, dislocations, or variations in the layer-spacing.[34, 35]. The

sharp peaks detected could be attributed to Silicon substrate and possibly the sample holder. Comparing the XRD results to the Raman data presented in the previous section, we observe an agreement that both techniques show the onset of crystallization of the SiC layers for growth temperatures of 600 °C and 950 °C. This is pretty much in agreement with the work of Said [16], although the onset of crystallization in that work was detected at 650 °C, i.e. 50 °C higher than our work here. That small discrepancy could be due to differences of the actual temperature of the substrate during growth or to the difference in the laser fluence (energy density) at the target.

4.5 Laser flash measurements

As mentioned before, the thermal properties and in particular, the thermal diffusivity of the three samples were determined using the laser flash technique. The three samples are sample 7, 13 and 14, deposited at 300 °C, 600 °C and 950 °C, respectively. For each frequency, the obtained data related to the magnitude and the phase are plotted as a function of relative beam position as shown in Figure 4.5 for sample 7 at 3500 Hz. These measurement were recorded for several frequencies as shown in Figure 4.6, for sample 7 the following frequencies 2000,3000, 3500, 4000, 4500, and 5000 Hz. For Sample 13 the measurements were recorded at the following frequencies 2000, 2500, 3000, 4000,and 5000 Hz. And for sample 14 the frequencies were 500, 700, 900, 1100, 1300, and 1500 Hz.

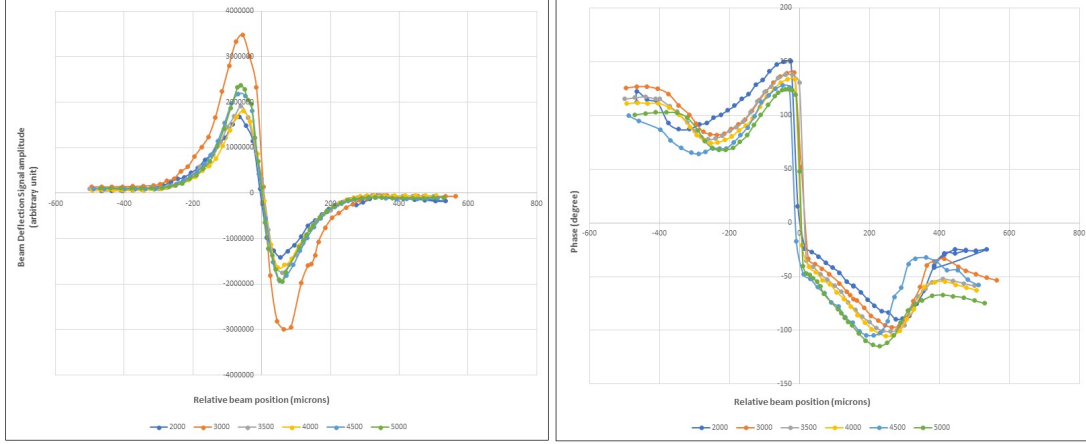


(a) Magnitude

(b) Phase

Figure 4.5: The (a) magnitude and (b) phase plots for sample 7 at frequency 3500 Hz

After checking that the obtained variations are symmetric, we calculate the slope of the region where the phase varies linearly, as shown in Figure 4.7. Since



(a) Magnitude

(b) Phase

Figure 4.6: The magnitude and phase plots for sample 7 at frequencies 2000,3000, 3500, 4000, 4500, and 5000 Hz

in the case of optically and thermal thick sample, the phase shifts approximately $\frac{27^\circ}{L_{th}}$. Hence from the slope, L_{th} is calculated by

$$L_{th} = \frac{27^\circ}{slope \times 10^{-6}} \quad (4.1)$$

We calculate the L_{th} for each measurement, as shown in Figure 4.8 for sample 7. After obtaining L_{th} for each frequency, we plot L_{th}^2 versus $1/\pi \cdot f$, as shown in Figure 4.9, where the slope of this plot is the thermal diffusivity on the sample according to equation 3.5.

As a result in sample 7 and 14 the laser flash measured the thermal diffusivity of the Si substrate. Since in sample 7 the SiC is amorphous, so there is no phonon resonance to stop the pump laser, hence it penetrates to the Si substrate heating it. Also sample 14 is too thin, thinner than the thermal wavelength, hence the Si substrate was measured. However, sample 13 the thermal diffusivity of SiC was measured, since it has a certain degree of crystallinity, so the pump laser is absorbed by phonon resonance and the SiC is heated. The value of the thermal diffusivity which is $1.14 \times 10^{-4} \text{ m}^2/\text{s}$ is a bit lower than the thermal diffusivity of pure crystalline 3C-SiC ($1.6 \times 10^{-4} \text{ m}^2/\text{s}$). The lower thermal diffusivity is most likely due to the fact that our sample 13 consists of a polycrystal and so grain boundaries would reduce the thermal diffusivity compared to that of a single crystal.

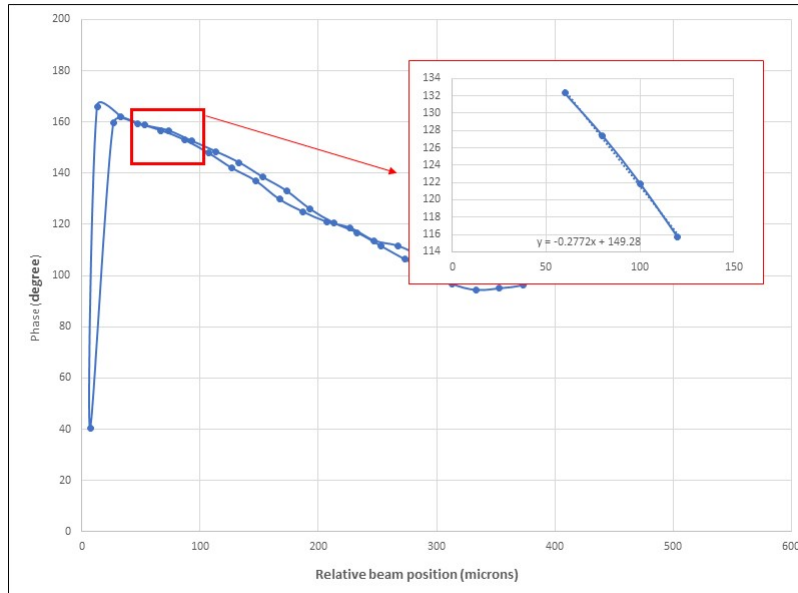


Figure 4.7: Slope of the phase in the linear region for sample 7 at frequency 3500 Hz

Frequency (Hz)	Phase's slope	L_{th} (m)	L_{th}^2 (m ²)	$1/\pi \cdot f$ (s)	slope of L_{th}^2 vs $1/\pi \cdot f$ (m ² /s)
			0	0	8.87E-05
2000	0.234	0.000115385	1.33E-08	0.000159236	
3000	0.2775	9.72973E-05	9.47E-09	0.000106157	
3500	0.2773	9.73675E-05	9.48E-09	9.09918E-05	
4000	0.3383	7.98108E-05	6.37E-09	7.96178E-05	
4500	0.3777	7.14853E-05	5.11E-09	7.07714E-05	
5000	0.4444	6.07561E-05	3.69E-09	6.36943E-05	

Figure 4.8: Data of sample 7, deposited at 300 °C

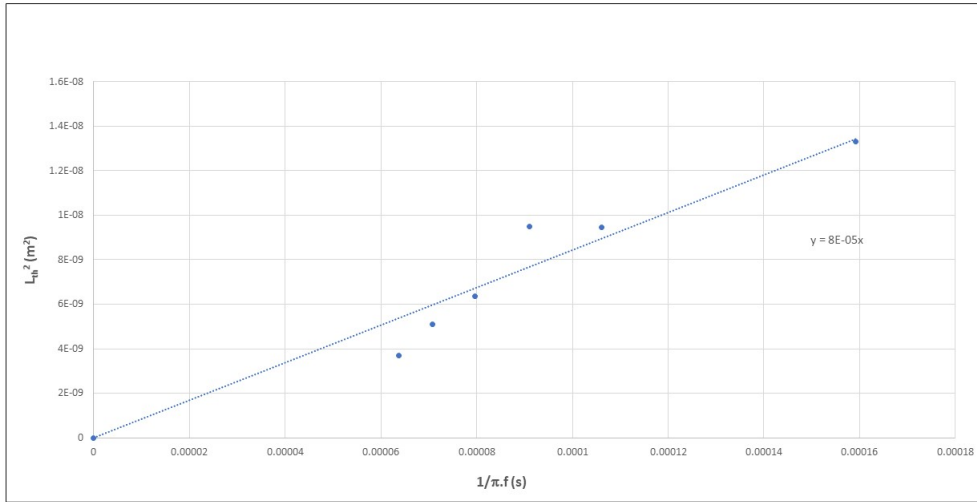


Figure 4.9: The plot of L_{th}^2 versus $1/\pi \cdot f$ for sample 7, deposited at 300 °C

Frequency (Hz)	Phase's slope	L_{th} (m)	L_{th}^2 (m ²)	$1/\pi \cdot f$ (s)	slope of L_{th}^2 vs $1/\pi \cdot f$ (m ² /s)
			0	0	1.14E-04
2000	0.1989	0.000135747	0.000159236	1.84E-08	
2500	0.2068	0.000130561	0.000127389	1.70E-08	
3000	0.211	0.000127962	0.000106157	1.64E-08	
4000	0.2248	0.000120107	7.96178E-05	1.44E-08	
5000	0.2424	0.000111386	6.36943E-05	1.24E-08	

Figure 4.10: Data of sample 13, deposited at 600 °C

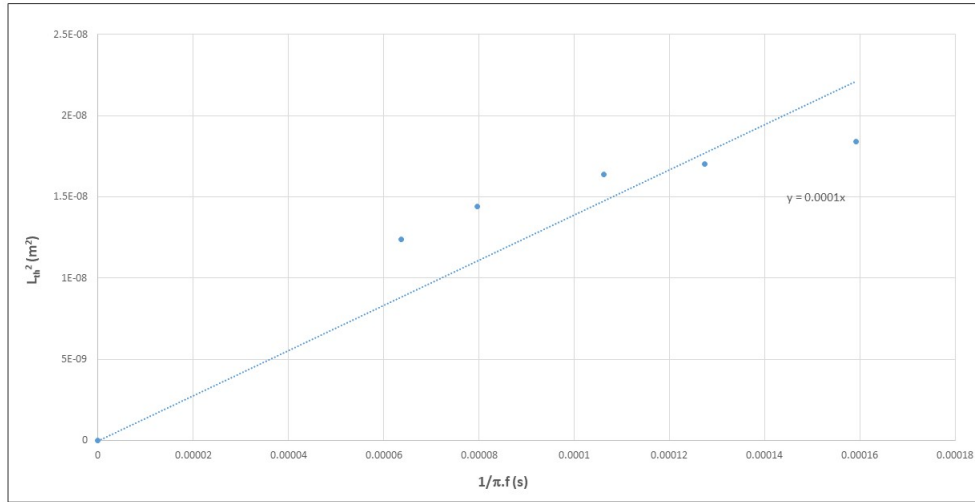


Figure 4.11: The plot of L_{th}^2 versus $1/\pi.f$ for sample 13, deposited at 600 °C

Frequency (Hz)	Phase's slope	L_{th} (m)	L_{th}^2 (m ²)	$1/\pi.f$ (s)	slope of L_{th}^2 vs $1/\pi.f$ (m ² /s)
			0	0	8.73E-05
500	0.1194	0.000226131	0.000636943	5.11E-08	
700	0.1315	0.000205323	0.000454959	4.22E-08	
900	0.1557	0.00017341	0.000353857	3.01E-08	
1100	0.167	0.000161677	0.000289519	2.61E-08	
1300	0.2392	0.000112876	0.000244978	1.27E-08	
1500	0.237	0.000113924	0.000212314	1.30E-08	

Figure 4.12: Data of sample 14, deposited at 950 °C

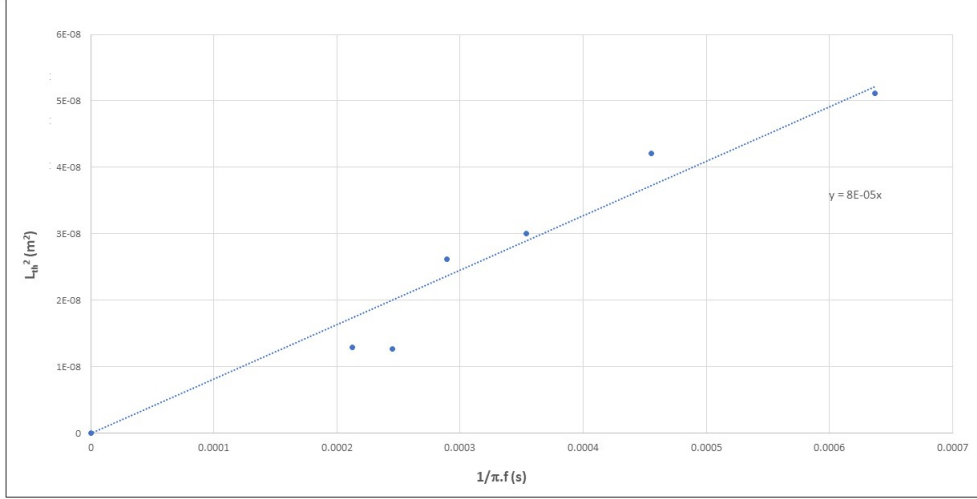


Figure 4.13: The plot of L_{th}^2 versus $1/\pi \cdot f$ for sample 14, deposited at 950 °C

Sample	Temperature of disposition (°C)	Sample thick-ness (nm)	Thermal Diffu-sivity (m^2/s)
sample 7	300	600	$8.87e^{-5}$
sample 13	600	400	$1.14e^{-4}$
sample 14	950	75	$8.73e^{-5}$

Table 4.3: Results Summary for sample 7,13, and 14, deposited at 300 °C, 600 °C, 950 °C, respectively

Chapter 5

Conclusion

In this thesis, we have achieved the synthesis of silicon carbide thin films on Si substrate by pulsed laser deposition with the aim of investigating their thermal properties as the nano-structure of the films transitions from amorphous to crystalline depending on growth conditions. The effects of the several experimental process parameters (laser repetition rate, growth pressure and temperature) on the nature of the grown films were revealed through several materials characterization techniques. Surface profilometry was used to measure film thickness and growth rate while surface morphology was imaged using Scanning Electron Microscopy (SEM). X-Ray Diffraction (XRD) and Raman Spectroscopy allowed the assessment of crystallinity and the determination of the type of bonding of the films, respectively. We used a photothermal-beam-deflection technique (laser flash) to determine the thermal diffusivity of the grown layers. Our study has led to the following conclusions:

- The synthesis process is reproducible and the growth rate depends almost linearly on laser repetition rate up to 25 Hz. Process controllability becomes problematic at higher repetition rate such as 50 Hz.
- Growth rate is significantly reduced at deposition pressures of 10 mTorr and above, due to the scattering of the ablated species by the background Ar gas.
- Deposition temperature plays a crucial role in determining the bonding configuration in the layers. At 300 °C, the grown layers are amorphous with the onset of crystallites formation detected at 600 °C. Fully crystallized layers are observed at 950 °C.
- The thermal diffusivity was determined at the onset of crystallization in the SiC layers, and a value of 1.14 cm²/s was reported, showing a significant enhancement compared to the Si substrate (0.88 cm²/s).

This work paves the way towards a full investigation of the evolution of the thermal properties of unhydrogenated silicon carbide materials as their nanostructure evolves from an amorphous to a fully crystalline state. Future perspectives include the determination of the thermal diffusivity of thicker SiC materials grown in the range between 600 and 950 °C, in order to correlate between film crystallinity and thermal transport. For the amorphous films, we propose performing laser flash measurements under grazing incidence configuration in order to enhance heat propagation in the films as opposed to the underlying Si substrate, resulting in the determination of the thermal diffusivity of amorphous SiC.

Bibliography

- [1] D. G. Cahill *et al.*, “Lower limit to the thermal conductivity of disordered crystals,” *Physical Review B*, vol. 46, 1992.
- [2] J. L. Feldman *et al.*, “Thermal conductivity and localization in glasses: Numerical study of a model of amorphous silicon,” *Phys. Rev.*, vol. 48, 1993.
- [3] a. o. Philip B. Allen, “Diffusons, locons and propagons: Character of atomic vibrations in amorphous Si,” *Philosophical Magazine*, vol. 79, 1999.
- [4] “Process technology for silicon carbide devices,”
- [5] S. G. B. Pecholta and P. Molian, “Review of laser microscale processing of silicon carbide,” *Journal of Laser Applications*, vol. 23, 2011.
- [6] G. Chen, “Nanoscale Energy Transport and Conversion: A Parallel Treatment of Electrons, Molecules, Phonons, and Photons,” 2005.
- [7] R. Peierls, “Selected Scientific Papers Of Sir Rudolf Peierls: (With Commentary),” *World Scientific*, 1997.
- [8] R. Peierls, “Quantum Theory of Solids,” *Oxford. Univ. Press*, 1955.
- [9] A. Einstein, “Elementare Betrachtungen über die thermische Molekularbewegung in festen Körpern,” *annalen der physik*, vol. 340, 1911.
- [10] G. A. Slack, “The Thermal Conductivity of Nonmetallic Crystals,” *Elsevier*, vol. 34, 1979.
- [11] M. T. Agne *et al.*, “Phase Transformation Contributions to Heat Capacity and Impact on Thermal Diffusivity, Thermal Conductivity, and Thermoelectric Performance,” *Advanced materials*, vol. 31, 2019.
- [12] P. B. Allen and J. L. Feldman, “Thermal conductivity of disordered harmonic solids,” *Phys. Rev.*, vol. 48, 1993.
- [13] W.-X. Zhou *et al.*, “Thermal Conductivity of Amorphous Materials,” *Advanced Functional Materials*, vol. 30, 2020.

- [14] M. C. Wingert *et al.*, “Thermal transport in amorphous materials: a review,” *Semiconductor Science and Technology*, vol. 31, 2016.
- [15] X. Cheng, “Overview of Recent Progress of Semiconductor Power Devices based on Wide Bandgap Materials ,” *Materials Science and Engineering*, 2018.
- [16] M.Tabbal, A.Said, and a. T. C. E.Hannoun, “Amorphous to crystalline phase transition in pulsed laser deposited silicon carbide,” *applied surface science*, vol. 253, pp. 7050–7059, 2007.
- [17] A. A. Lebedev, “Heterojunctions and superlattices based on silicon carbide,” *Semiconductor Science and Technology*, vol. 21, no. 1, pp. 17–34, 2006.
- [18] N. Ault, “Silicon carbide ceramics, structure and properties of,” *Encyclopedia of Materials: Science and Technology*, pp. 8502–8508, 2001.
- [19] P. Masri, “Silicon carbide and silicon carbide-based structures the physics of epitaxy,” *Surface science reports*, vol. 48, pp. 1–51, 2002.
- [20] e. a. H. Krebs, and M. Weisheit, “Pulsed Laser Deposition (PLD) - a Versatile Thin Film Technique,”
- [21] E. Morintale *et al.*, “Thin Films Development by Pulsed laser-assisted deposition,” *Physics AUC*, vol. 20, pp. 43–56, 2010.
- [22] M. Ohring, “Thin-Film Evaporation Processes,” *Materials Science of Thin Films*, 2002.
- [23] C. W. Schneider and T. Lippert, “Laser Ablation and Thin Film Deposition,” *Laser Processing of materials*, 2010.
- [24] M. Balooch *et al.*, “Deposition of SiC fUms by pulsed axeimer laser ablation,” *Appl. Phys. Lett*, vol. 57, 1990.
- [25] MING.Y.CHEN and P. MURRAY, “Deposition and characterization of SiC and cordierite thin films grown by pulsed laser evaporation ,” *Journal of Materials Science*, vol. 25, pp. 4929–4932, 1990.
- [26] M. A. Capano *et al.*, “Pulsed laser deposition of silicon carbide at room temperature ,” *Appl. Phys. Lett*, vol. 64, 1994.
- [27] L. Rimai *et al.*, “Pulsed laser deposition of SiC films on fused silica and sapphire substrates ,” *Journal of Materials Science*, vol. 73, 1993.
- [28] G. Soto *et al.*, “Growth of SiC and SiCxNy films by pulsed laser ablation of SiC in Ar and N2 environments,” *Journal of Vacuum Science & Technology*, vol. 16, 1998.

- [29] P. N.Prasad, "Nanophotonics," 2004.
- [30] C. V. RAMAN *et al.*, "A New Type of Secondary Radiation," *Nature*, vol. 121, 1928.
- [31] a. R. M. S. Gurvinder Singh Bumrah, "Raman spectroscopy – Basic principle, instrumentation and selected applications for the characterization of drugs of abuse," *Egyptian Journal of Forensic Sciences*, vol. 6, 2016.
- [32] M. A. Olmstead *et al.*, "Photothermal Displacement Spectroscopy" An Optical Probe for Solids and Surfaces," *Applied Physics*, vol. 32, 1983.
- [33] Y. Inoue, S. Nakashima, and A. Mitsuishi, "Raman Spectra Of Amorphous SiC," *Solid State Communications*, vol. 48, 1983.
- [34] E. López-Honorato *et al.*, "Control of stoichiometry, microstructure, and mechanical properties in SiC coatings produced by fluidized bed chemical vapor deposition," *Journal of Materials Research*, vol. 23, 2008.
- [35] A. Ortiz *et al.*, "X-ray powder diffraction analysis of a silicon carbide-based ceramic," *Materials Letters*, vol. 49, 2001.

